



Review

Current status and future directions of all-solid-state batteries with lithium metal anodes, sulfide electrolytes, and layered transition metal oxide cathodes

Chaoshan Wu^{a,1}, Jiatao Lou^{b,1}, Jun Zhang^b, Zhaoyang Chen^a, Akshay Kakar^a, Benjamin Emley^c, Qing Ai^d, Hua Guo^d, Yanliang Liang^c, Jun Lou^d, Yan Yao^{a,c,*}, Zheng Fan^{e,**}

^a Materials Science and Engineering Program, University of Houston, Houston, TX 77204, USA

^b College of Materials Science and Engineering, Zhejiang University of Technology, Hangzhou 310014, PR China

^c Department of Electrical and Computer Engineering and Texas Center for Superconductivity at the University of Houston (TcSUH), University of Houston, Houston, TX 77204, USA

^d Department of Materials Science and NanoEngineering, Rice University, Houston, TX 77005, USA

^e Department of Engineering Technology, University of Houston, Houston, TX 77204, USA

ARTICLE INFO

Keywords:

All-solid-state battery
Lithium metal anode
Sulfide electrolyte
Layered transition metal oxide cathode

ABSTRACT

All-solid-state batteries (ASSBs) offer great promise as a next-generation energy storage technology with higher energy density, wider operating temperature range, and improved safety for electric vehicles. ASSBs employing lithium metal anodes (Li), sulfide-based solid-state electrolytes (SSE), and Ni-rich layered transition metal oxide cathodes (LiMO_2 , $M = \text{Ni, Mn, Co, Al}$) are particularly promising due to its superior electrochemical performance compared to other solid-electrolyte systems. However, the battery cycle life at high cathode mass loading and high current is still limited because the failure mechanism is not fully understood. Lithium dendrite growth at the anode or inside a solid electrolyte still represents as a serious risk of cell failure. Interfacial resistance increases attributed to electrolyte decomposition and interfacial void formation at both cathode–electrolyte and anode–electrolyte interfaces lead to gradual capacity fading. In this Review, we present the fundamental challenges and recent scientific understandings of each component in ASSBs. The novel diagnostic tools for these components, especially the interfaces buried under the surface that are often hard for characterization are mainly examined. Finally, we offer a perspective for future research directions. We hope this Review will provide a timely snapshot of state-of-the-art research progress in ASSBs to accelerate the development of ASSBs.

1. Introduction

The replacement of internal-combustion-engine-based vehicles with electric vehicles (EVs) is a growing trend and an essential solution to address carbon emission issues and climate change. The U.S. Department of Energy's Battery500 consortium aims to boost battery specific energy to 500 Wh kg^{-1} , almost double that of today's typical EV battery, which ranges from 200 to 250 Wh kg^{-1} [1]. However, the 500 Wh kg^{-1} target is difficult to reach using conventional Li ion batteries (LIBs) because they use graphite anodes, organic liquid electrolytes (LE), and lithium metal oxide cathodes (e.g., LiCoO_2) [2–5]. As shown in the overview of LIB development (Fig. 1), the classical graphite-liquid

electrolyte- LiCoO_2 architecture was established in the 1990 s, after which novel anode, electrolyte, and cathode batteries with higher safety, longer life, and more stable performance were pursued. Attempts to enhance performance included replacing graphite anodes with Li metal anodes to dramatically improve energy density [6–8] and the use of Ni-based layered metal oxides, such as $\text{LiNi}_x\text{Mn}_y\text{Co}_z\text{O}_2$ (NMC, $x + y + z = 1$) and $\text{LiNi}_{0.8}\text{Co}_{0.15}\text{Al}_{0.05}\text{O}_2$ (NCA), as cathode materials [9–12]. These Ni-rich cathode materials have favorable specific capacity, rate capability, and working voltage. Li-NMC and Li-NCA batteries encapsulated with organic liquid electrolytes have a high material-level energy density (considering the weight of active materials) and have a theoretical specific energy reaching 1000 Wh kg^{-1} [13,14]; thus,

* Corresponding author at: Materials Science and Engineering Program, University of Houston, Houston, TX 77204, USA.

** Corresponding author.

E-mail addresses: yyao4@central.uh.edu (Y. Yao), fanzheng@central.uh.edu (Z. Fan).

¹ These authors contributed equally to the work.

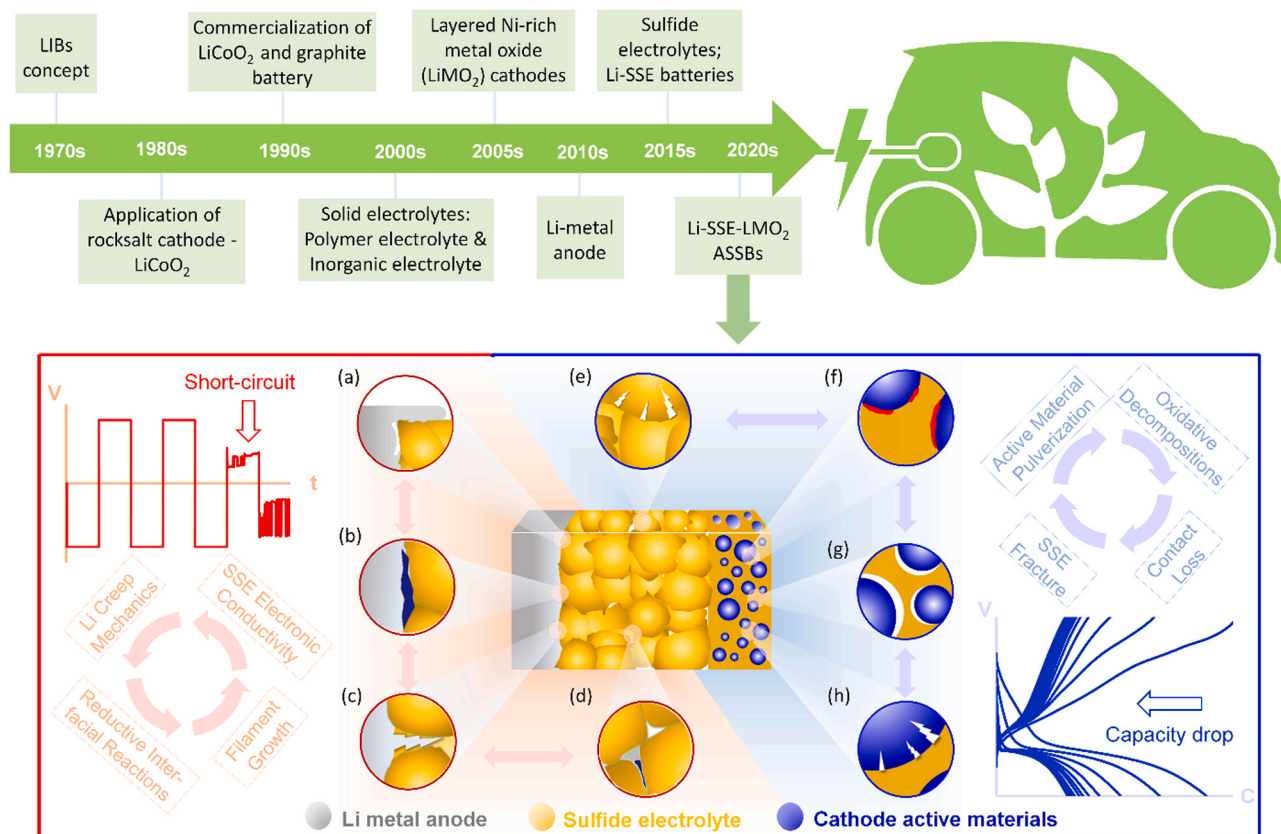


Fig. 1. Overview of LIB development, practical challenges of ASSBs, and Li-SSE-LiMO₂ architecture. (a) Contact elastoplasticity of the Li metal. (b) Reductive interfacial reactions. (c) Dendrite growth. (d) Electrochemical instability within the SSE. (e) Mechanical failures of the SSE. (f) Oxidative electrolyte degradations. (g) Void generations due to the contact loss between the cathode particles and the solid electrolyte after cycling. (h) Structural instability of the cathode.

cell-level specific energy may reach 500 Wh kg⁻¹ with a 50% decrease from packing assembly [15]. Together with progress in electrode materials, the development of solid-state electrolytes (SSEs) for LIBs addresses safety concerns in flammable liquid electrolyte solutions and potentially improves energy density [16–21]. Moreover, SSEs in the battery promise enhanced safety and high-energy densities that are desired for EV applications. Unfavorable side reactions at the interface between the liquid electrolyte and Li anode, such as solid electrolyte interphase (SEI) formation and Li filament growth, will likely be resolved at the solid-solid Li/SE interface [17,22]. Mainstream SSEs include polymetric, inorganic oxide, and sulfide electrolytes. The polymetric electrolytes show excellent cathodic stability than oxide electrolytes, but anodic stability is lower [23,24]. Sulfide electrolytes present narrower electrochemical voltage window as compared with polymetric or oxide competitors [25]. Among these SSEs, polymer-based electrolytes feature good chemo-mechanical wettability of the interface, enabling favorable contact with electrodes during fabrication and battery operation [19,26–28]. Low mechanical stiffness of polymer-based electrolytes absorbs mechanical impacts from the electrode upon battery charge-discharge, preventing internal physicochemical failure of the ASSB. However, polymer electrolytes suffer from multiple drawbacks, including inferior mechanical stability, poor stability at elevated temperatures, and a narrow electrochemical stability window [29–31]. The typical polymer electrolyte framework, such as poly (ethylene oxide) (PEO), possesses a low ionic conductivity in the range of 10⁻⁶–10⁻⁸ S cm⁻¹ at room temperature. In addition, Li dendrite growth in polymer electrolytes is more severe than in inorganic solid electrolytes [32], which is attributed to the low-shear modules of polymer electrolytes [33–35]. Conversely, the large-shear moduli of inorganic electrolytes (e.g., oxide-based electrolytes at usually $Y_G > 8$ GPa) inhibit metal dendrite growth [36]. For example, improved garnet-type,

oxide-based electrolytes can reach a high ionic conductivity of 10⁻³–10⁻⁴ S cm⁻¹ [37]. However, large-shear moduli of garnet inorganic electrolytes can lead to mechanical fracture failures due to strain from battery cycling [38]. The shear moduli of “softer” sulfide SSEs are lower than garnet-type inorganic electrolytes but still higher than those of polymer electrolytes [39–41]. Thus, the use of sulfide SSEs in Li-LiMO₂ electrode battery systems can mitigate fracture failure [42–45]. Moreover, sulfide conductors show extraordinarily high ionic conductivities (~10⁻² S cm⁻¹) that compare with those of organic liquid-based electrolytes [42,46]. These advantages make SSEs ideal solid electrolyte candidates for use with Li-LiMO₂ electrodes for high-energy ASSBs targets. The electrochemical capacitive performance of recently reported Li-SSE-LiMO₂ batteries is summarized in Table 1.

Despite the benefits of using SSEs and Li-LiMO₂ electrode systems, several academic and commercial challenges must be addressed before their large-scale use. As illustrated in Fig. 1, general issues of the Li-SSE-LiMO₂ architecture include: 1) Li metal anode: contact elastoplasticity (Fig. 1a); 2) Li-SSE anode interface: interfacial reactions (Fig. 1b) and dendrite growth (Fig. 1c); 3) SSE: electrochemical instability (Fig. 1d) and mechanical failures (Fig. 1e); 4) SSE-LiMO₂ interfaces: oxidative electrolyte degradation (Fig. 1f) and void generation (Fig. 1g); and 5) LiMO₂ cathodes: structural instability (Fig. 1h). In the following sections, we will provide an overview of recent studies of these topics and offer our perspectives on the practical applications of Li-SSE-LiMO₂ batteries.

2. Li metal anodes

Li metal is a promising anode candidate for rechargeable ion batteries due to its high theoretical capacity (3860 mAh g⁻¹) [6,7]. Li metal anodes provide approximately 50% higher battery energy density than

Table 1
Electrochemical performance of Li-SSE-LiMO₂ ASSBs.

Battery composition			Capacity	Year & Refs
SSE	Anode	Cathode		
Li ₆ PS ₅ Cl	Li-In	NMC ₇₁₁	153.4 mAh g ⁻¹ (0.1 C, 0.312 mA cm ⁻² , 25 °C)	2020 [47]
Li ₆ PS _{4.7} O _{0.3} Br	Li-In	NMC ₈₁₁	108.7 mAh g ⁻¹ (0.1 C, 0.214 mA cm ⁻² , 25 °C)	2019 [48]
Li _{5.7} Zn _{0.15} PS _{4.85} O _{0.15} Br	Li-In	NMC ₈₁₁	98 mAh g ⁻¹ (0.1 C, 0.214 mA cm ⁻² , 25 °C)	2019 [49]
Li ₆ PS ₅ Br	Li-In	NMC ₁₁₁	150 mAh g ⁻¹ (0.1 C, 0.13 mA cm ⁻² , 25 °C)	2019 [50]
Li ₆ PS ₅ Cl	Li-In	NMC ₁₁₁	80 mAh g ⁻¹ (0.1 C, 0.066 mA cm ⁻² , 25 °C)	2017 [51]
Li ₆ PS ₅ Cl	Li-In	NCA	147 mAh g ⁻¹ (0.1 C, 0.05 mA cm ⁻² , 25 °C)	2019 [52]
Li ₆ PS ₅ Cl	Li-In	NMC ₁₁₁	122 mAh g ⁻¹ (0.1 C, 0.1 mA cm ⁻² , 25 °C)	2020 [53]
Li ₆ PS ₅ Cl	Li-In	NMC ₇₁₁	150 mAh g ⁻¹ (0.1 C, 0.12 mA cm ⁻² , 30 °C)	2020 [54]
Li ₆ PS ₅ Cl	Li-In	NCA	140 mAh g ⁻¹ (0.1 C, 0.12 mA cm ⁻² , 25 °C)	2020 [55]
Li ₆ PS ₅ Cl	Li	NMC ₈₁₁	98.6 mAh g ⁻¹ (0.1 C, 0.06 mA cm ⁻² , 30 °C)	2018 [56]
Li _{6.55} P _{0.45} Si _{0.55} S ₅ I	Li	NMC ₈₁₁	90 mAh g ⁻¹ (0.1 C, 0.02 mA cm ⁻² , 30 °C)	2020 [57]
Li ₃ PS ₄	Li	NMC ₆₂₂	144 mAh g ⁻¹ (0.1 C, 0.178 mA cm ⁻² , 25 °C)	2020 [58]
Li ₃ PS ₄	Li-In	NMC ₁₁₁	150 mAh g ⁻¹ (0.05 C, 0.064 mA cm ⁻² , 25 °C)	2020 [59]
Li ₃ PS ₄	Li-In	NMC ₈₁₁	176 mAh g ⁻¹ (0.1 C, 0.214 mA cm ⁻² , 25 °C)	2020 [60]
Li ₃ PS ₄	Li-In	NMC ₁₁₁	166 mAh g ⁻¹ (0.05 C, 0.064 mA cm ⁻² , 25 °C)	2020 [61]
Li ₃ PS ₄	Li-In	NMC ₁₁₁	120 mAh g ⁻¹ (0.1 C, 0.13 mA cm ⁻² , 25 °C)	2020 [62]
Li ₃ PS ₄	Li	NMC ₆₂₂	170.1 mAh g ⁻¹ (0.1 C, 0.12 mA cm ⁻² , 55 °C)	2018 [63]
Li ₃ PS ₄	Li-In	NMC ₆₂₂	140 mAh g ⁻¹ (0.1 C, 0.053 mA cm ⁻² , 30 °C)	2017 [64]
Li ₃ PS ₄	Li-In	NCA	133.5 mAh g ⁻¹ (0.1 C, 0.074 mA cm ⁻² , 25 °C)	2019 [65]
Li _{9.54} Si _{1.74} P _{1.44} S _{11.7} Cl _{0.3}	Li-In	NMC ₆₂₂	175.7 mAh g ⁻¹ (0.1 C, 0.2 mA cm ⁻² , 40 °C)	2020 [66]
Li ₁₀ GeP ₂ S ₁₂	Li-In	NCA	176.0 mAh g ⁻¹ (0.05 C, 0.093 mA cm ⁻² , 40 °C)	2020 [67]
Li ₁₀ GeP ₂ S ₁₂	Li-In	NMC ₈₁₁	163.1 mAh g ⁻¹ (0.1 C, 0.204 mA cm ⁻² , 35 °C)	2020 [68]
Li ₁₀ GeP ₂ S ₁₂	Li-In	NCA	146 mAh g ⁻¹ (0.1 C, 0.075 mA cm ⁻² , 25 °C)	2016 [69]
Li ₁₀ GeP ₂ S ₁₂	Li-In	NCA	119.2 mAh g ⁻¹ (0.1 C, 0.063 mA cm ⁻² , 25 °C)	2020 [70]

do conventional graphite anodes [71]. In solid-state batteries, Li metal anodes can reduce space-weight requirements while guaranteeing a high energy density [72]. Moreover, Li metal anodes are more chemically stable against SSEs than are liquid-based electrolytes, which addresses most negative effects that conventionally occur in liquid batteries, such as dendrite formation-induced safety concerns [8]. However, many unknown aspects of Li metal anodes may impede the success of Li metal ASSBs at the device level [6,7]. Notably, plastic volume deformation of

Li metal during electrochemical cycling is challenging for Li/SE “solid-solid” contact, resulting in interface void formation and even anode delamination at high-current densities (> 3 mAh cm⁻²) [73–75]. Therefore, investigation of Li metal electrochemical-chemo-mechanical effects, especially Li creep behaviors, on battery cycling are critical for controlling stability of the Li anode. Fundamental investigations of these mechanisms are currently in progress.

2.1. Mechanical properties of Li metal based on bulk and small-scale measurements

Pharr et al. reported the mechanical response of Li metal using a tensile test. The stress-strain relationship in bulk Li over a wide range of strain rates from 5⁻⁴ (1/s) to 5⁻¹ (1/s) is shown in Fig. 2(a) [76]. Tensile tests show that rate-sensitive deformation of Li metal and its steady-state flow condition can be reached at room temperature and indicate potential dendrite morphology control through deformation mechanics. A similar deformation study of Li metal reported by Sakamoto et al. [77] indicated a strain-rate plasticity of Li under pressure, suggesting creep is a dominant deformation mechanism in battery-relevant situations. The major focus of this study was the prevention of arbitrary incremental displacement and strain in Li metal that induces plastic creeping on the Li/SE interface. Their time-dependent (creep) deformation tests of Li confirmed that frictional force-induced hydrostatic stress on the Li metal contact surface can impede Li metal deformation and prevent internal short-circuit resulting from Li flow over the interface (Fig. 2b). Studies of sample aspect ratio effects and adhesive Li forces have significant implications for other alkali metals (e.g., Na, K) that serve as battery anodes. In addition to the intrinsic mechanical properties of Li metal, interactions between the SSE and bulk Li can also induce mechanical failure of the Li anode. Anand et al. has established a model of Li anode response in ASSBs based on large deformation theory [80]. This model simulates the interaction between the Li anode and SSE upon elastic-viscoplastic response of the Li and indicates that relevant viscoplastic properties, including plastic-elastic distortion, elastic strain, and stress, dominate the bulk Li response. This work also provides important evidence that strain-rate revulsion is a major inducer of Li anode volume deformation-related battery failure, with size-dependent yield strength of the Li also contributing to this effect. Particularly, the porous nature of electrodeposited Li and its related dendrites render an undesired stress architecture. As measured by bulk tensile and nano-indentation tests, Li metal exhibits significant strain-rate sensitivity and size dependency on creeping. This information can enable the fine-tuning of deformation mechanics by adjusting Li deposits to improve robustness of the Li anode and mitigate unstable Li growth during electrochemical cycling [76].

In addition to Li metal anode bulk mechanics studies, the investigation of nano-mechanics yields more detailed surface and local information at a small-length scale. These small-scale measurements provide valuable insight into nano- and microscale Li metal deformation and can offer new perspectives for probing the morphological and mechanical behaviors that occur on the Li anode surface. Nano-indentation is one of the most commonly used tools for surface and local area characterization [81]. When the Li nano-indentation test is implemented in an inert gas environment [78,82–85], coupled mechanical, electrochemical, and morphological behaviors can be comprehensively analyzed (Fig. 2c) [78]. Herbert et al. reported a series of nano-indentation work on high-purity vapor-deposited Li film [83–85]. Data regarding plastic flow properties, including the elastic modulus, hardness, and yield strength, and their evolution together with key variables such as length scale, strain rate, temperature, crystallographic orientation, and electrochemical cycling were collected. Here, the plastic flow behavior of Li is primarily related to steady-state creep under constant load or stress, a common scenario for the Li anode in battery application [86,87]. Li creep upon electrochemical charge-discharge can induce buckling at the interfaces and generate addition stress, which together with Li

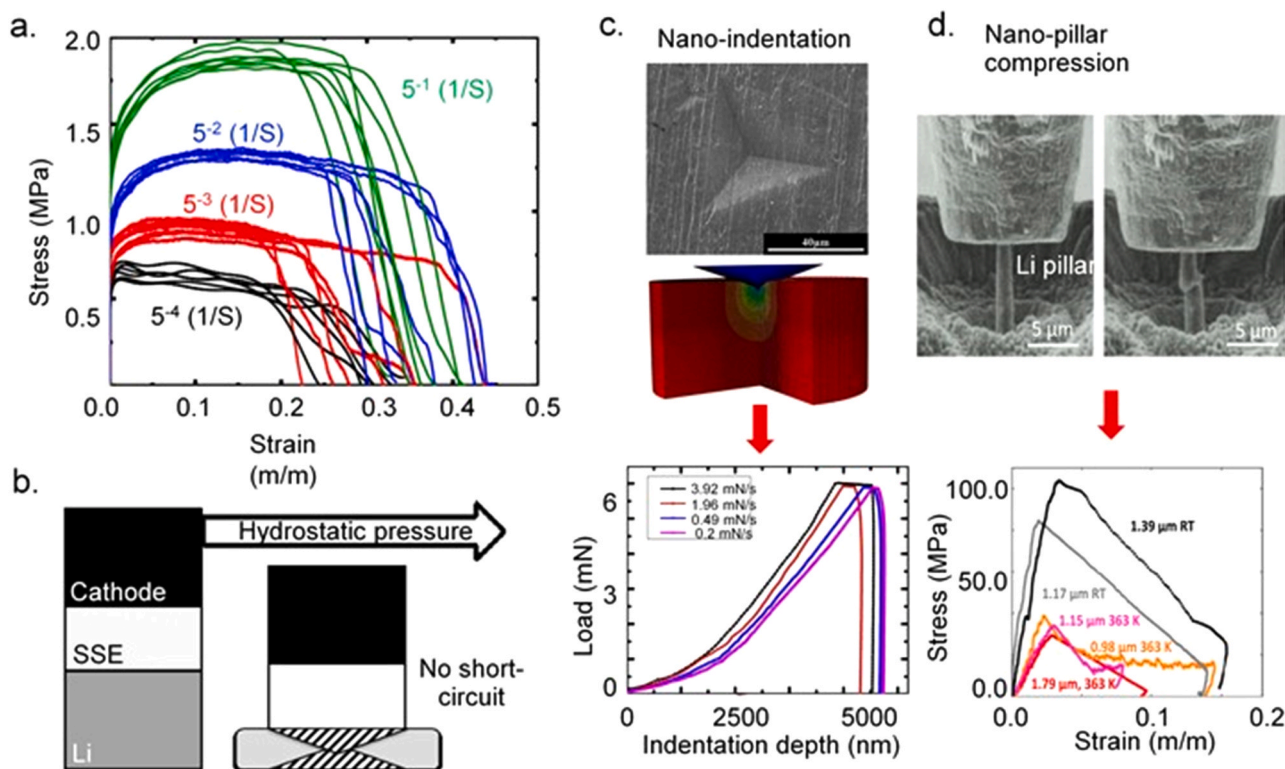


Fig. 2. Li metal mechanical properties. Bulk measurements: (a) Stress-strain relationship from uniaxial tension testing of bulk Li metal at nominally constant strain rates of 5^{-1} (1/s), 5^{-2} (1/s), 5^{-3} (1/s), and 5^{-4} (1/s). (b) Frictional force in Li/current collector and Li/SE interfaces create hydrostatic stresses that impede deformation, preventing Li flow and short-circuiting. Small-scale measurements: (c) Nano-indentation load-depth curves with different loading rates. (d) *In situ* compression of a representative 1- μ m diameter Li pillar.

(a) Reproduced with permission [76]. ©2019, Elsevier. (b) Reproduced with permission [77]. ©2018, Springer Nature. (c) Reproduced with permission [78]. ©2016, Elsevier. (d) Reproduced with permission [79]. ©2016, American Association for the Advancement of Science.

viscoplastic behavior can further impact the interface contact area, resulting in ion diffusion channel deterioration and interface instability. However, current nano-mechanical investigations on Li metal are still preliminary. More progress is needed toward coupling studies of the mechanical properties of Li as a function of sample dimensions, temperature, crystallographic orientation, and contact conditions. To this end, several novel surface and local measurement techniques, such as nano-pillar compression [79], have been proposed for analyzing coupling at Li metal anode interfaces. Nano-pillar compression studies can provide insight into critical issues such as power-law creep, stress-strain behavior, and viscoplastic deformation, among others, as shown in Fig. 2(d). Moreover, novel nano-mechanical techniques, such as *in situ* real-time observations of Li nano-mechanics, can provide high-fidelity information regarding mechanical failure, thus enabling fundamental understanding of morphological-mechanical coupling effects and allowing the rational design of nano- and microscale Li metal anodes.

2.2. Li metal failures during battery operation

In parallel with experimental investigations, a number of theoretical evaluations have confirmed the significance of mechanical instabilities in Li metal anodes, especially contact mechanic failures between Li metal and SSEs. Such works include a Li metal dendrite model reported by Monroe and Newman [33–35], contact mechanics models [90,91], and interface kinetic models [88,92,93]. Among these studies, the Monroe-Newman model was established based on Li metal and polymer electrolyte architecture (Fig. 3a) and considered factors such as elasticity of the electrolyte, compression forces, surface tension, and deformation forces. This model predicts that the Li filament will not be

productive if the electrolyte has a sufficiently high shear modulus [34, 35]. However, it is theoretically possible to avoid the dendrite problem. Work by Chiang et al. indicates that a high shear modulus will result in a high critical current density (CCD) that induces Li metal fill-up and filament propagation [41,94]. Therefore, a high elastic modulus of the electrolyte cannot address the metallic filament growth problem and may raise new challenges, such as decreased ionic conductivity of the electrolyte, which would impede the battery's proper function. For a broader modeling analysis of the Li contact surface, contact mechanic models have focused on correlations between contact area and squeezing force [90,91] and have derived the boundary conditions that affect stress distribution functions for elastic, elastoplastic, and adhesive contacts on the Li metal anode. Based on this model, the contact area at the Li/SSE interface can be predicted, thus providing a tool to study ion diffusion at the interface and contact area loss-induced capacity drop. Different than the dendrite growth model, which is built upon linear elasticity theory, the interface kinetic model analyzes contact stresses and as-induced effective current density distributions [88,92,93] (Fig. 3b). The interface kinetic model can predict several critical issues of Li metal anodes, including the evolution of mechanical stress and stress-induced electrochemical potential changes. The interface kinetic models also allows for incorporation of microstructural heterogeneity and brittle fracture of SSEs to properly understand dendrite growth [33–35,90,91], further extending the scope of probing Li anode reaction mechanisms.

All of the described models were generally established in a static mechanical context with constant compression and surface conditions. The evolution of the Li anode upon electrochemical cycling is a synthetic process characterized by creeping, plating-stripping effects, and elastoplasticity changes. For example, the competition between creeping and

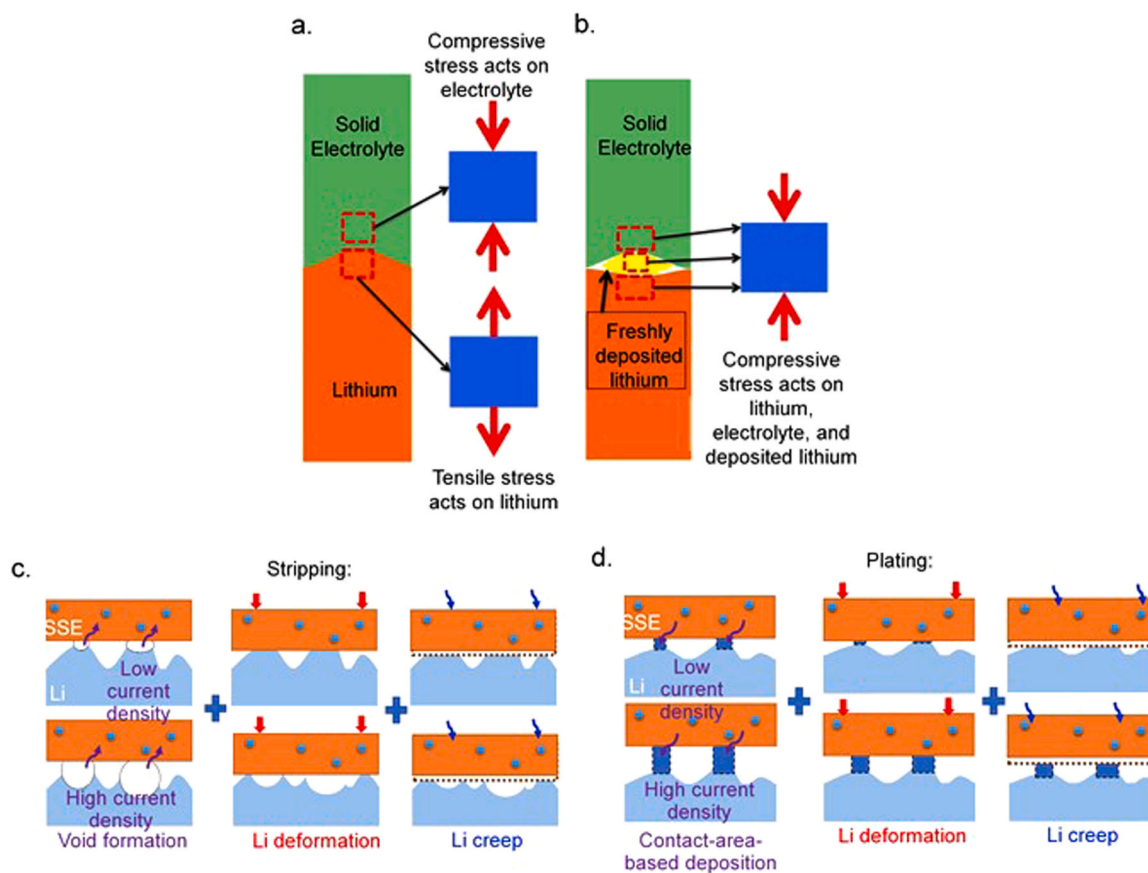


Fig. 3. Li metal anode failure mechanisms. Schematic representations of two scenarios observed at the Li/SSE interface in a static contact model: (a) Pre-stressed lithium metal analyzed by Monroe and Newman and (b) Relaxed initial state of Li metal. Dynamic pressure-driven model: (c) Li stripping with creep. White and blue circles represent stripped Li and Li ions, respectively. Purple arrows denote Li ion stripping, red arrows stack pressure, and blue arrows creep effect. (d) Competition between Li plating and creep. Blue columnar regions show the newly deposited Li, and small circles represent Li ions. For (c) and (d), purple arrows denote Li ion stripping, red arrows stack pressure, and blue arrows creep effect.

(a, b) Reproduced with permission [88]. ©2017, Electrochemical Society. (c, d) Reproduced with permission [89]. ©2020, Cell Press.

electrodeposition under pressure dominates the Li metal contact stress and contact area [95]. A series of theoretical analyses and experimental studies have shown the morphological transformations of Li anodes upon coupling effects [77,89,95,96]. Fig. 3(c) presents the evolutions of void formation due to stripping and contact pressure at low current density ($I = 0.05 \text{ mA cm}^{-2}$), where the asperity height contact initially increases but then decreases due to Li creep, forming a conformal contact. Fig. 3(c) also shows that, at a sufficiently high current density ($I = 5 \text{ mA cm}^{-2}$), stripping induces electrochemical Ostwald ripening [8, 97], resulting in contact loss that cannot be filled by metal deformation (creep). In this case, increased stack pressure can diminish the void to maintain a stable contact area. However, a higher stacking pressure leads to a dynamically stable contact region due to the increasing effects of Li creep, but the accelerated deformation of Li metal over time may enhance void generation.

Time-course Li plating and creeping dynamics under the combined effects of current density and stack pressure are shown in Fig. 3(d). As Li ions can only be deposited on the contact area, and the deposition rate is proportional to current density, the Li metal incremental height is restricted to the contact region. At low current density ($I = 0.005 \text{ mA cm}^{-2}$), the newly deposited Li will be flattened by elastoplastic deformation and time-dependent creep. In contrast, deposition induced by high current densities will exceed Li creep effects, resulting in a columnar growth morphology between the Li metal and SSE [89] that initiates Li dendrites during charging. Therefore, we can conclude that creep only dominates contact behavior at low current densities. In high current density cases, Li metal contact conditions are more

influenced by Li plating-stripping effects.

For our review of these recent advances of Li metal anodes in ASSBs, we do not restrict the discussion to applications of Li anodes with sulfide-based electrolytes. Various Li metal anode mechanical property investigations, from bulk mechanical response tests to nano-mechanic studies, and both static and dynamic contact mechanic models are summarized. Generally, three types of interactions between Li metal and SSE are present [98], including creep buckling, brittle fracture, and dendrite penetration. These potential mechanical failures shed light on the design of anodes for sulfide-based SSEs. Due to the brittle nature of the sulfide composites, contact interactions with the anode at the interface are critical for improving battery reversibility.

Numerous approaches have been proposed to address Li metal anode challenges, mitigate how Li metal creeping impacts the battery, and establish an intimate and stable contact with the SSE. First, theoretical calculations by Harris indicated that a high stack pressure of $\sim 20 \text{ MPa}$ tends to suppress void formation and may be a promising approach for ensuring consistent lithium metal contact for stable cell performance [89]. Alternatively, strategies such as elastic polymer coating [99–102] and hybrid membrane interlayers [103–105] have also been useful in fine-tuning Li anode contact mechanics. Despite these potential advances, further research is needed to comprehensively understand the contact mechanics of Li metal under stack pressure. Second, novel Li alloying strategies [106] may address porosity and void formation issues upon anodic reaction. Li alloys allow manipulation of pure Li mechanical properties to optimize Li/SSE contact and improve ion transport at high current densities [107,108]. In recent studies, by adjusting the In:Li

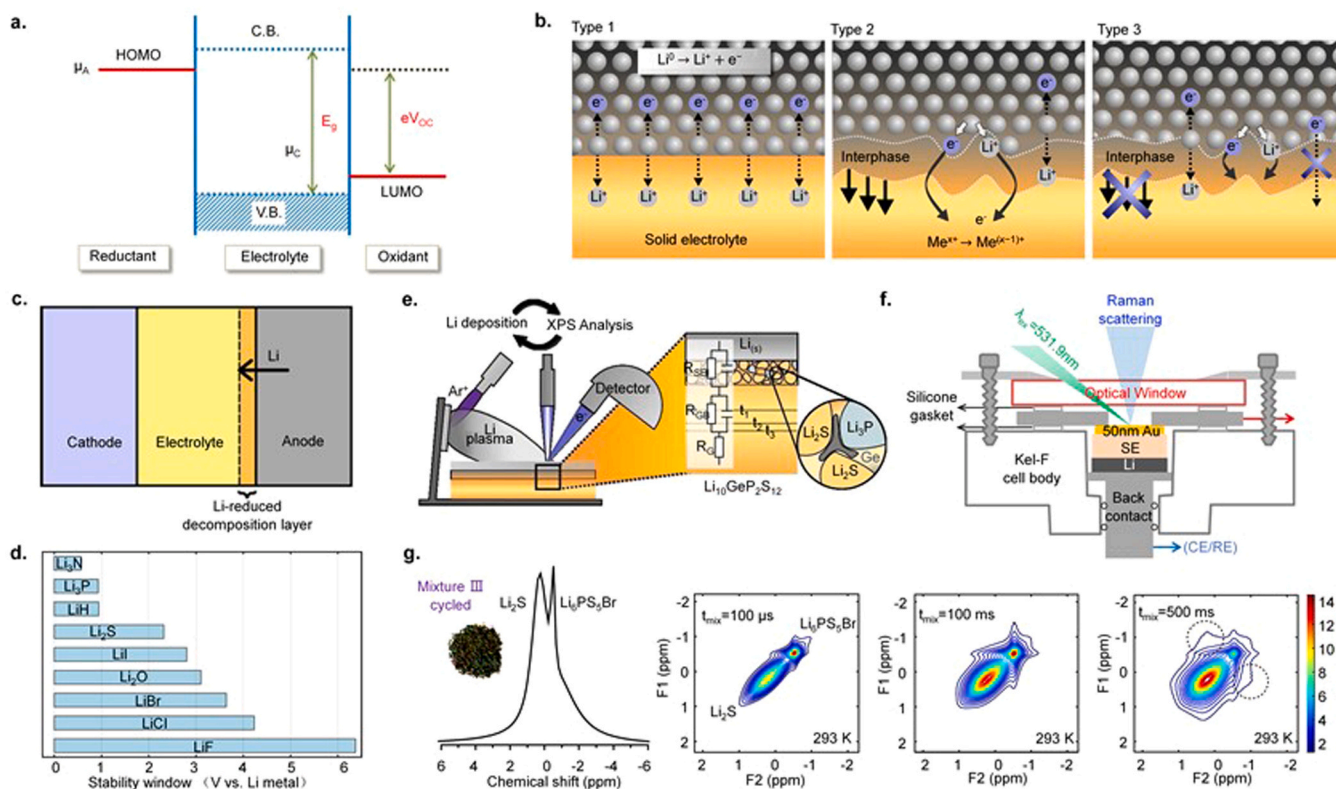


Fig. 4. Li/SSE interface electrochemical stabilities and typical experimental measurements: (a) Stable energy window diagram for SSEs. (b) Interfaces between Li metal and SSE. Type 1: Non-reactive and thermodynamically stable; Type 2: Reactive and mixed conducting; and Type 3: Reactive and metastable SEI. (c) Schematic of a full cell showing reduction of the electrolyte by the Li metal anode. (d) Electrochemical stability ranges of Li binary compounds. When available, these ranges are computed from experimental thermodynamic data. (e) Experimental setup of an *in situ* X-ray photoelectron spectroscopy experiment to monitor the reaction between sulfide and Li. (f) Spectro-electrochemistry cell designed for operando Raman spectroscopic measurements at the SSE and thin film metal electrode interface. (g) NMR measurement of spontaneous Li ion transport between the Li₆PS₅Br SSE and Li₂S cathode after cycling. One dimensional (1D) Li magic angle spinning (MAS) spectrum of the cycled Li₆PS₅Br-Li₂S cathode mixture III (mixed nano-Li₂S). Two-dimensional Li-Li exchange spectra (2D-EXSY) measured under MAS at a resonance frequency of 330.39 MHz and spinning speed of 30 kHz at 298 K for the cycled mixture III at $t_{\text{mix}} = 100 \mu\text{s}$, 100 ms, and 500 ms are shown. (a) Reproduced with permission [116]. ©2009, American Chemical Society. (b) Reproduced with permission [118]. ©2015, Elsevier. (d) Reproduced with permission [111]. ©2016, American Chemical Society. (e) Reproduced with permission [117]. ©2016, American Chemical Society. (f) Reproduced with permission [120]. ©2017, American Chemical Society. (g) Reproduced with permission [121]. ©2017, The Authors, published by Springer Nature Publishing AG.

mass ratio, a Li-In alloy shows a higher redox potential (0.62 V) against the Li⁺-Li couple, enabling a stable chemical window with the sulfide Li₃PS₄ SSE [109]. In addition, Li-Mg alloys have been shown to effectively mitigate void generation and also provide the advantage of a reduced stack pressure requirement [106]. Third, contact elastoplasticity induces electrolyte decomposition and ultimately gives rise to a high interfacial resistance, thus generating a beneficial interface between Li and sulfide-based electrolytes, which can be harnessed a practical solution to address the electrochemical-mechanical challenges of Li metal anodes and promote overall battery performance.

3. Li-SSE interface

Sulfide-based electrolytes coupled with Li metal anodes in ASSBs demonstrate increased energy density and superior ionic conductivity. However, Li-SSE interfaces experience some practical challenges, such as irreversible electrolyte decomposition and Li dendrite formation. Moreover, the poor solid-solid contact between Li metal and sulfide electrolytes causes severe crack/gap issues [110,111]. To address these challenges, recent investigations of the Li-SSE interface have focused on improving electrochemical and thermodynamic stability and comprehensively understanding interfacial ion conduction and interface reactivity [112–117].

During cycling, the Li-SSE interface undergoes various physical and chemical changes, such as nucleation, SEI formation, and dendritic

growth. These coupled transformations significantly impact electronic performance and cycling stability. Xu et al. define the interfacial reactions as the combination of energy status, defects, and contacts [118]. As shown in Fig. 4(a), the thermodynamically stable operating “window” is represented by E_g , which is the energy separation between the lowest unoccupied molecular orbital (LUMO) and highest occupied molecular orbital (HOMO) of the electrolyte. The interface will be unstable if the chemical potential for the cathode (μ_c) is below HOMO and that of the anode (μ_a) is above LUMO, unless an SEI is formed. Wenzel et al. interpret these interfacial reactions from the perspective of thermodynamic instability [116], as shown in Fig. 4(b) and have categorized Li/SSE anode interphase formation into three types:

- 1) The SEs such as LLZO and LLTO are in thermodynamic equilibrium with Li [119]. Thus, no reactions.
- 2) Thermodynamic instability between Li and SE is present, which causes chemical reactions between Li and SE and generates a mixed conducting interphase (MCI) [122]. The MCI conducts both ions and electrons. Classic examples of MCI include LGPS and the NASICON-type SSEs, such as Li_{1+x}Al_xTi_{2x}(PO₄)₃ (LATP) and Li_{1+x}Al_xGe_{2-x}(PO₄)₃ (LAGP). This interphase type continuously expands and grows into the SSE during battery operation. As a result, electrons pass through the electrolyte due to changes in bulk electrolyte properties, which leads to self-discharge of the battery. This case typically applies to SSEs composed of multivalent cations.

Various studies have been conducted to avoid this interface reaction by adding an artificial SEI layer to act as a barrier to the Li metal [123,124].

- 3) Thermodynamic instability between Li and SE is present, but the interfaces react to form an SEI that conducts ions but blocks electrons [125]. A few examples of these interfaces include Li-stuffed garnet (LLZO), LiPON, and $\text{Li}_7\text{P}_3\text{S}_{11}$ (LPS).

In fact, most sulfide-type SSEs exhibit unstable interface pairing to Li metal. Due to the unique electrochemical, mechanical, and structural properties of sulfide electrolytes, three major challenges exist related to Li-SSE interfaces, including high-impedance interface, mechanical failures, and Li dendrite growth, which limit breakthroughs associated with ASSBs.

3.1. High-impedance interface layer formation

Richards et al. calculated the electrochemical stability window of several types of SSE against Li metal, among which the voltage stability window of sulfide SSEs is narrow [111], as shown in Fig. 4(c) and (d). They concluded that interface stability is mainly determined by the stability window of the relevant binary system; for mixed anion materials, the least stable binary unit, such as Li_2S to $\text{Li}_6\text{PS}_5\text{Cl}$, is critical. The binary unit Li_nX ($n = 1, 2, 3$, X = anion) is generated before the formation of the phase equilibrium product during charge-induced decomposition, followed by the extraction of Li from Li_nX ($n = 1, 2, 3$, X = anion). For Li extraction to occur, the formation energy of Li_nX and the mixing energy of other binary materials must be exceeded. Typically, the mixing energy is relatively low, and the reduction potential of the electrolyte is close to that of the binary intermediate product. However, polyanionic electrolytes show a wider stable voltage window due to their strong bonds, which raise the Li extraction barrier. Lepley et al. studied the Li/SSE interface decomposition process using first principle calculation [126] and found that Li/ Li_3PO_4 has a more stable interface than Li/ Li_3PS_4 , indicating that P—O has a stronger bond than P—S. They also explored the decomposition process of γ - Li_3PS_4 and β - Li_3PS_4 , their calculations indicated the deterioration of P—S bonds of γ - Li_3PS_4 . Similar behavior was observed for β - Li_3PS_4 at the first few cycles, and cycling continued with the Li metal anode due to the formation of a stable thin buffer layer that prevented further decomposition of β - Li_3PS_4 . Wagemaker et al. have performed more detailed studies of the decomposition route for typical SSEs. For example, they reported that the most favorable decomposition pathway for the argyrodite $\text{Li}_6\text{PS}_5\text{Cl}$ is indirect lithiation, rather than direct decomposition to the most thermodynamically stable product [127]. The practical electrochemical stability window of $\text{Li}_6\text{PS}_5\text{Cl}$ is determined by the oxidation (delithiation) and reduction (lithiation) potentials of $\text{Li}_4\text{PS}_5\text{Cl}$ (S/S^{2-} redox at 2.24 V) and $\text{Li}_{11}\text{PS}_5\text{Cl}$ (through the P/P^{5+} redox at 1.08 V), respectively. The delithiated phase rapidly decomposes into stable Li_3PS_4 , S and LiCl, and the lithiated phase into P, Li_2S , and LiCl. A similar decomposition process was predicted by Goddard et al., who studied Li/ $\text{Li}_6\text{PS}_5\text{Cl}$ interface decomposition through quantum-based reactive molecular dynamics simulations [128], a powerful *ab initio* computational method used to describe crystalline structural transformations during the chemical reaction. This state-of-the-art simulation approach revealed a quick decomposition at the Li/ $\text{Li}_6\text{PS}_5\text{Cl}$ interface that can be attributed to the weak S-P bond and with decomposition products that contain Li_3P , Li_2S , LiCl, and possibly LiP. These low ionic conductive decomposition products diminish ion transportation at the interface.

In contrast to theoretical calculations, experimental investigations of interfacial decomposition are rather challenging, as the reaction site is sandwiched at the bulk interface. Some pioneering studies, however, have overcome these difficulties using advanced *in situ* techniques to provide an in-depth understanding of the high-impedance interface formation process. As shown in Fig. 4(e), Janek et al. monitored the SEI formed between Li metal and $\text{Li}_{10}\text{GeP}_2\text{S}_{12}$ using time-resolved

electrochemical measurements and *in situ* X-ray photoelectron spectroscopy (XPS) [117]. They observed that impedance of a symmetrical battery greatly increases with time and is ascribed to interfacial decomposition of $\text{Li}_{10}\text{GeP}_2\text{S}_{12}$. The decomposition comprises Li_3P , Li_2S , and Li—Ge alloys, which were detected by XPS. They also monitored the formation of phases between $\text{Li}_7\text{P}_3\text{S}_{11}$ and Li metal by similar methods [129] and identified Li_2S and Li_3P as the decomposition products. For more detailed compositional studies on interface formation, Nuzzo et al. examined the structure and reactivity of β - Li_3PS_4 and $\text{Li}_{10}\text{GeP}_2\text{S}_{12}$ during Li plating and stripping by *in situ* Raman spectroscopy, together with XPS and SEM [120], as shown in Fig. 4(f). A partially reversible conversion of PS_4^{3-} to $\text{P}_2\text{S}_6^{4-}$ was found for β - Li_3PS_4 , while LGPS only showed irreversible changes at potentials lower than 0.7 V vs. Li^+/Li . Based on the aforementioned work, the same group introduced two interlayer materials, Si and $\text{Li}_x\text{Al}_{(2-x/3)}\text{O}_3$ (LiAlO), at the $\text{Li}_7\text{P}_3\text{S}_{11}$ (LPS)/Li interface and evaluated their electrochemical properties. Both interlayers could eliminate the inherent LPS decomposition that occurs on the Li surface before cycling. LiAlO could inhibit the decomposition process of LPS by reducing the potential between LPS and Li, while LPS at the interface was reduced to Li_2S after cycling when a Si interlayer was present. The lithiated Si interlayer maintained strong reduction potential, which caused LPS reduction at the interface. Using non-destructive two-dimensional Li ion exchange solid-state nuclear magnetic resonance (2D exchange NMR) (Fig. 4g), Wagemaker et al. carried out a fundamental study of Li ion transport at the interface [121]. Their NMR results indicate that the interface ion conductivity between the two materials is heavily dependent on the preparation method of the mixture. Damage of the interface contact during the charge-discharge cycle was also observed, which resulted in decreased interface ion conductivity.

3.2. Mechanical failures at the interface

In addition to interfacial chemical reactions, mechanical failures induced by fabrication, stacking pressure, or internal pressure resulting from volume changes are also detrimental to the stability of the anode interface [6118]. Although applied pressure during battery fabrication and operation promotes contact between SSEs and Li metal, the interface is subjected to mechanical failure due to surface and internal defects of bulk SSEs or the Li anode. Bruce et al. studied the processes of plating and stripping on the Li/ $\text{Li}_6\text{PS}_5\text{Cl}$ interface [107] by employing a three-electrode setup to quantitatively measure the contributions of plating or stripping to interface transformations. They found that, when the stripping current density is high, voids are generated in the Li metal at the interface. Because lithium metal creep replenishes at the interface, voids formed during the previous stripping are covered. The described studies indicate that interface voids produced by stripping are key factors that intensify uneven lithium deposition. Moreover, stack pressure impacts the creep properties of Li metal, thereby affecting the CCD. Ultimately, the occurrence of voids reduces the contact area at the interface and increases local current density, which results in dendrite formation and an internal short-circuiting.

3.3. Dendrite growth at the Li/SSE interface

Monroe and Newman proposed that because the elasticity modulus of a polymer membrane is two times greater than that of a Li filament, Li cannot penetrate through the SSEs due to linear-elastic deformation [35]. However, various SSE designs used in multiple studies that consider this possibility have failed to produce a long-lasting battery because numerous inorganic SSEs, such as sulfides and garnets, enable a higher modulus of elasticity than Li metal [112,115,130–132], are prone to dendrite penetration, and cause short-circuiting during electrodeposition. Previously, the CCD test was widely employed to evaluate an SSE's resistivity to a Li filament. By increasing the current density in a stepwise manner, the CCD is determined by short-circuiting of the battery, an indicator of Li filament formation. However, this test fails to

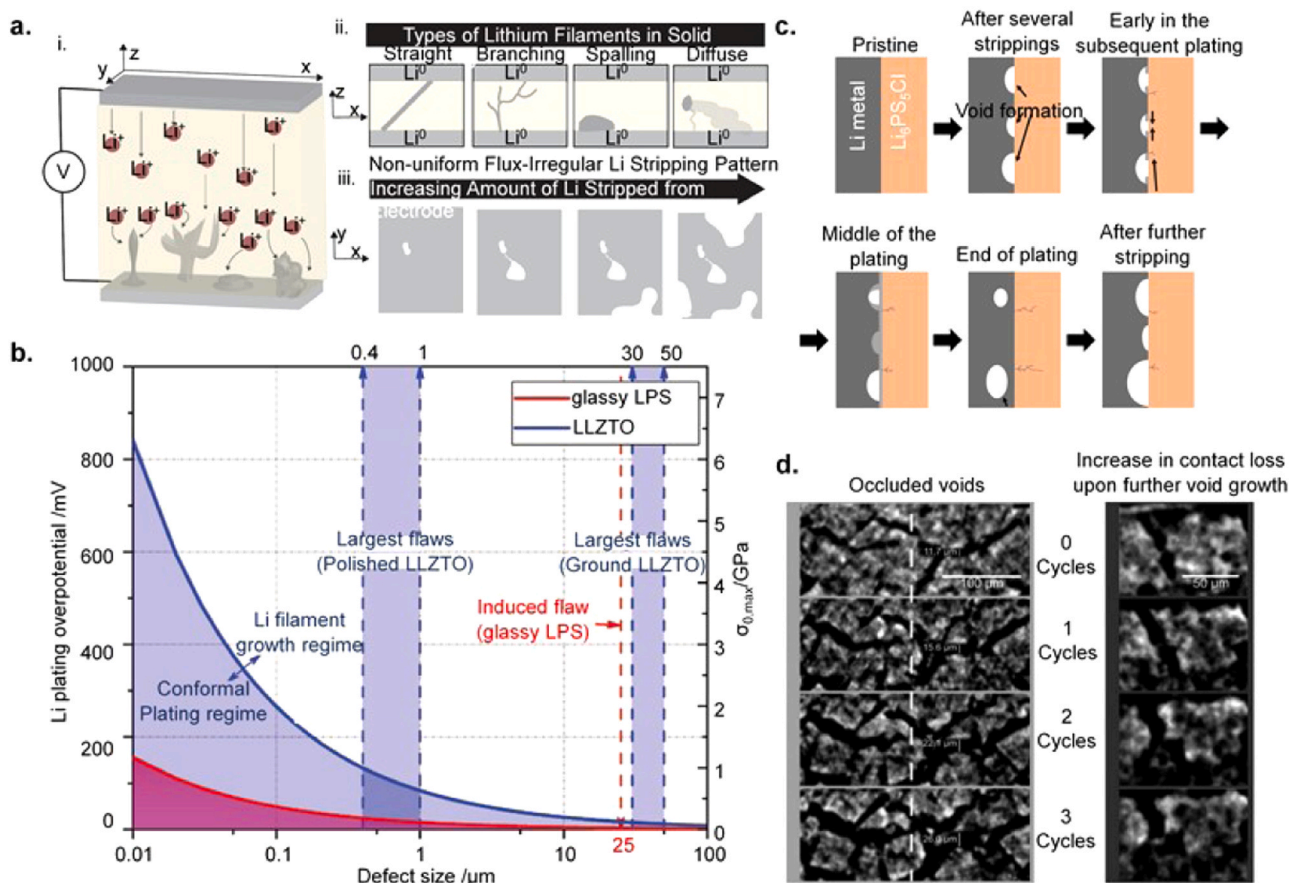


Fig. 5. (a) Li metal filament. i. The schematic of Li filament growth in SSEs. ii. Four-types of Li filament penetration. iii. Irregular stripping of the Li metal causes irregular interfaces at high discharge rates. (b) Inverse square root dependence of Li plating overpotential and crack-extension stress ($\sigma_{0, \max}$) on defect size. Curves for glassy LPS and LLZTO are shown. Vertical lines correspond to the large-flaw population of the indicated experimental samples. (c) Schematic of Li/Li₆PS₅Cl interface cycled at an overall current density above the critical current for stripping. (d) Early-stage synchrotron-based X-ray tomography monitoring of void expansion and Li evolution in a symmetric cell with β -Li₃PS₄ SSEs cycled at 100 $\mu\text{A cm}^{-2}$.

(a) Reproduced with permission [134]. ©2020, Elsevier. (b) Reproduced with permission [139]. ©2017, Wiley-VCH. (c) Reproduced with permission [107]. ©2019, The Authors, published by Springer Nature Publishing AG. (d) Reproduced with permission [140]. ©2018, Electrochemical Society.

fully capture the dynamic nature of Li filament formation. Thus, *in situ* and operando experiments during electrochemical cycling are needed to reveal Li nucleation and growth mechanisms. Dasgupta et al. observed several Li filament growth modes (straight, branching, spalling, and diffuse) in an LLZO SSE using an operando visualization technique during battery cycling [133,134], as shown in Fig. 5(a). Similar modes (straight and spalling) were observed in glassy LPS. This work also demonstrated interfacial evolutions at high discharge rates. Non-uniform Li stripping upon deep discharge was ascribed to high local current densities at the Li/SSE interface, which leads to vacancy accumulation and void formation, thus creating irregular interfaces. Although some investigations aim to improve ionic conductivity and prevent Li penetration by modifying electrolyte composition, this goal has not yet been achieved [135–137]. One known limitation of the Monroe-Newman model is its assumption that the interface is flat and smooth. However, this assumption only holds for electrolytes that inherently form smooth surfaces, such as vapor-deposited LiPON [110]. Because sulfide-based electrolytes in bulk batteries are not vapor-deposited, this model does not provide reliable results. Typically, for SSEs, mechanical failure occurs due to pre-existing defects at the interface known as Griffith flaws [138]. Fig. 5(b) plots the defect size's influence on Li plating overpotential and crack-extension stress ($\sigma_{0, \max}$) [139]. Both curves are inverse proportional functions of LLZTO and glassy LPS, indicating that overpotential and $\sigma_{0, \max}$ decrease with an inverse square root dependence on defect size. In bulk batteries,

interfacial flaws are the initial sites that become occupied by Li metal during electrodeposition. With all gaps filled, further Li metal deposition pushes it into the electrolyte layer. This penetration leads to widening and propagation of the initial flaw, providing additional space for more Li metal deposition. Bruce et al. investigated the separate processes of Li plating and stripping at the Li/Li₆PS₅Cl interface using three-electrode cells [107]. Based on *in situ* X-ray computed tomography imaging and SEM, they proposed a model for Li/Li₆PS₅Cl interface evolution during cycling. After several stripping events, evident voids formed. In early plating, they found that Li plating began at the point where the Li metal, SSE and void meet and then grew along the free surface of the void. Voids were cut off from the interface and occluded within the Li metal due to growth of the film in the middle of the plating. At the end of plating, some unfilled voids became isolated and were forced away from the interface. These voids accumulated during cycling and were exposed at the interface after further stripping, leading to increasing loss of contact. Using operando synchrotron X-ray tomography, Seitzman et al. studied Li evolution in a Li/LPS/Li cell before and after cycling [140]. After one cycle, the dark line features, which represented the boundaries between LPS grains, widened and continued to widen in the next few cycles. In parallel, LPS grain structure was disrupted due to continued Li growth.

In situ acoustic studies conducted by Sakamoto et al. on Li penetration mechanisms indicated that SSEs lose stiffness during Li penetration as a result of crack propagation [138]. Moreover, Xu et al. demonstrated

Table 2

Characteristic parameters of typical solid-state electrolytes at room-temperature.

Composition	State	Ionic conductivity (S·cm ⁻¹)	Activation energy (eV)
50Li ₂ S-50GeS ₂	Glass	4 × 10 ⁻⁵	0.51
60Li ₂ S-40SiS ₂	Glass	5.3 × 10 ⁻⁴	0.33
67Li ₂ S-33 P ₂ S ₅	Glass	10 ⁻⁴	0.36
Li ₇ P ₃ S ₁₁	Glass-Ceramic	3.2 × 10 ⁻³	0.125
Li ₇ P ₃ S ₁₁	Glass-Ceramic	1.7 × 10 ⁻²	0.18
Li ₃ PS ₄	Glass-Ceramic	2.8 × 10 ⁻⁴	0.356
78Li ₂ S-22 P ₂ S ₅	Glass-Ceramic	1.78 × 10 ⁻³	0.31
80Li ₂ S-20 P ₂ S ₅	Glass-Ceramic	7.2 × 10 ⁻⁴	0.25
Li ₇ Ge ₃ PS ₁₂	Crystal	1.1 × 10 ⁻⁴	0.26
Li _{3.25} Ge _{0.25} P _{0.75} S ₄	Crystal	2.2 × 10 ⁻³	0.207
Li _{9.54} Si _{1.74} P _{1.44} S _{11.7} Cl _{0.3}	Crystal	2.5 × 10 ⁻²	0.238
Li ₁₀ GeP ₂ S ₁₂	Crystal	1.2 × 10 ⁻²	0.21
Li ₁₀ SnP ₂ S ₁₂	Crystal	4 × 10 ⁻³	0.87
Li ₁₀ SiP ₂ S ₁₂	Crystal	2.3 × 10 ⁻³	0.20
Li ₁₁ AlP ₂ S ₁₂	Crystal	8 × 10 ⁻⁴	0.263
Li ₆ PS ₅ Cl	Argyrodite	1.3 × 10 ⁻³	0.33
Li ₆ PS ₅ Br	Argyrodite	10 ⁻²	0.20

that, at nanoscale, dendrites possess a higher yield strength than the external pressure applied, which leads to propagation through the electrolyte, rather than buckling [79]. Therefore, rational design of interfaces between Li metal and sulfide-based electrolytes may be a solution for preventing Li penetration.

The application of an artificial SEI between Li metal and SSE has been intensively studied, with the goal of inhibiting undesirable side reactions, as well as Li penetration at the interface. Sun et al. introduced a solid-state plastic crystal electrolyte (PCE) as an interlayer between Li metal and LGPS [141], which prevents direct contact and thereby prevents reduction reactions or decompositions at the interface. They also synthesized a Li_xSiS_y protective layer with good air stability and high ionic conductivity for the Li₃PS₄/Li interface [142]. The composition of this protective layer and its protection mechanism were explored by in-depth synchrotron-based, high-energy XPS analysis, which found that the all-solid-state Li / Li₃PS₄ / LiCoO₂ battery with a Li_xSiS_y protection layer on the anode interface shows good cycle performance over 100 cycles.

4. Sulfide-based SSEs

Sulfide composites represent a promising family of materials for SSE generation. Sulfide-based electrochemical electrolytes have demonstrably remarkable room temperature ionic conductivity (~10⁻² S cm⁻¹) comparable to that of conventional carbonate-based liquid electrolytes [28,45]. Other characteristics of sulfide materials, such as their robust mechanical properties, are also favorable for sulfide-based electrolyte application [55]. Table 2 presents the characteristic parameters of representative sulfide electrolytes [43]. According to structural and ion conduction mechanisms, three major types of sulfide-based electrolytes have been categorized, including glass-glass-ceramic Li₂S-P₂S₅ [143], crystal thio-LISICON Li_{4-x}Ge_{1-x}P_xS₄ (0 < x < 1) [144], and argyrodite type Li₆PS₅X (X = Cl, Br, I) [145]. The crystalline structure of these three types of sulfides are shown in Fig. 6. However, their performance in ASSBs are only minimally acceptable due to their poor electrochemical stability and the unstable rigid interface between SSEs and electrode materials [46]. Moreover, the unsuccessful scale-up fabrication of the separator layer based on extreme atmosphere-sensitive sulfide materials impedes the commercialization

of sulfide-based electrolytes [146]. Here, we summarize the challenges and trends of three major types of sulfide-based electrolytes relevant to the application of ASSBs.

4.1. Electrochemical stability challenges related to sulfide electrolytes

An electrolyte with a broad electrochemical stability window is critical for building a high-energy-density ASSB and mitigating side reactions, such as SEI formation. The electrochemical windows of sulfide-based electrolytes show remarkable stabilities, ranging from 0 to 5 V vs. Li [147–149]. However, these windows were overestimated in early measurements due to flawed testing protocols. The conventional half-cell configuration (Li/SE/metal) limits the true performance of kinetic energy [150]. Therefore, in addition to experimental investigations, theoretical calculations of the electrochemical window can provide an in-depth understanding of the electrochemical stability of sulfide electrolytes. Zhu et al. investigated intrinsically thermodynamically stable electrochemical windows and predicted potential decomposition products for common sulfide electrolytes using density functional theory computations [151]. This study revealed a much narrower stability window of sulfide electrolytes compared with previous experimental measurements, suggesting a highly favorable decomposition reaction between Li and sulfide-based electrolytes. Their decomposition during cycling leads to further growth of an electronically conductive SEI layer that induces cell capacity decay and increases impedance. As shown in Fig. 6(a), most of sulfide electrolytes has a decomposition energy within 1.5–2.5 eV [151]. However, some decomposed products are stable against the Li metal with high μ_{Li}, enabling a stability window beyond the reduction potential (Fig. 6b). For example, reduction of the typical glass-ceramic Li₃PS₄ (stoichiometrically 0.75Li₂S-0.25 P₂S₅) occurs at 1.71 V, in which the thermal-equilibrium reduction product is Li₂S. The oxidation of Li₃PS₄ starts at 2.31 V and results in P₂S₅. Similar to Li₃PS₄, the argyrodite Li₆PS₅Cl is also reduced at 1.71 V, with the reduction products Li₂S and LiCl, but its oxidation occurs at a lower voltage (2.01 V) to produce Li₃PS₄ and LiCl, followed by the oxidation of Li₃PS₄ at 2.31 V into P₂S₅. For the crystalline thio-LISICON sulfide (Li_{4-x}Ge_{1-x}P_xS₄ (0 < x < 1)), including Li₁₀GeP₂S₁₂ (LGPS) and Li_{3.25}Ge_{0.25}P_{0.75}S₄, the stable electrochemical window is calculated as 1.71–2.1 V. The reduction of thio-LISICONs occurs below 1.71 V, which results in the lithiation products Li₄GeS₄ and Li₂S. Next, the binary compound Li₄GeS₄ will be further reduced at 1.62 V, eventually decomposing to high-impedance Li₂S. The oxidation of thio-LISICONs starts at 2.14 V, generating Li₃PS₄ and GeS₂ as delithiation products. The continued decomposition of the binary compound also occurs during oxidation. At a higher oxidation voltage (2.31 V), Li₃PS₄ is further oxidized to P₂S₅. Han et al. has reported a combined computational and experimental study of LGPS to verify its electrochemical window [152]. Using an in-house Li/SE/SE-carbon cell setup, authentic reduction and oxidation cyclic voltammetry (CV) LGPS plots were generated and were comparable to thermodynamic predictions (Fig. 6c).

The discrepancy of electrochemical properties among glass-glass-ceramic, crystal, and argyrodite sulfides are attributed to the unique lattice structure of these compounds. Li₃PS₄ (0.75Li₂S-0.25 P₂S₅) is a typical glass-glass-ceramic sulfide with high ionic conductivity (10⁻³ S cm⁻¹) at room temperature [153,154] and is regarded as the most stable (100 - x) Li₂S-xP₂S₅ binary system. As shown in Fig. 7(a), different arrangements of PS₄³⁻ tetrahedrons in Li₃PS₄ result in three crystal phases [25], namely α-Li₃PS₄, β-Li₃PS₄, and γ-Li₃PS₄. During the electrochemical reaction between metallic Li and Li₃PS₄, local Li⁺ depletion of the sulfide electrolyte results in the reduction of PS₄³⁻ and formation of Li₂S and P₂S₆⁴⁻. In contrast, during oxidation, P₂S₆⁴⁻ consumes Li₂S and is transformed to PS₄³⁻ with the oxidation of Li⁰. The reduction and oxidation of PS₄³⁻ in Li₃PS₄ can be illustrated in the following reactions [120].

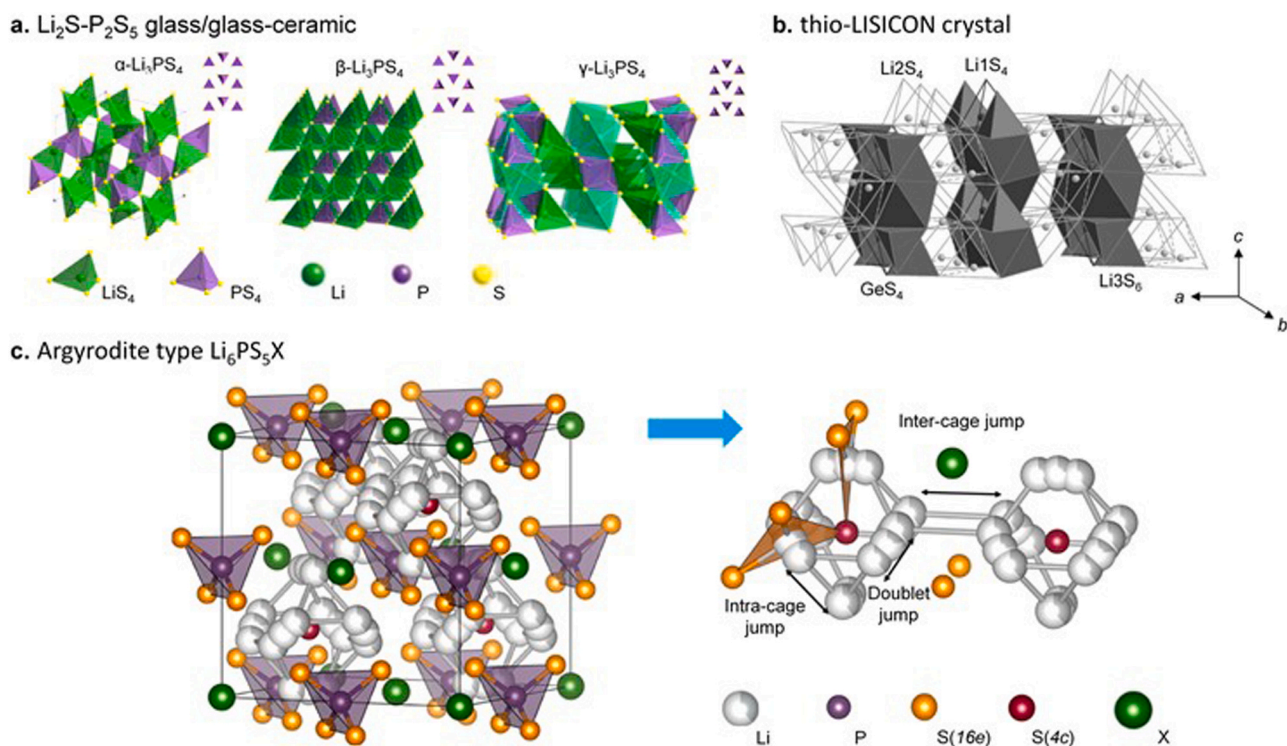


Fig. 7. The crystalline structure of common sulfide-based electrolytes. (a) Crystal structure of α - Li_3PS_4 , β - Li_3PS_4 , and γ - Li_3PS_4 . (b) Crystal structure of Li_4GeS_4 . (c) Crystal structure of argyrodites $\text{Li}_6\text{PS}_5\text{X}$ ($\text{X} = \text{Cl}, \text{Br}, \text{I}$). (a) Reproduced with permission [153,154]. ©2010, Physical Society of Japan. (b) Reproduced with permission [155]. ©2002, Elsevier. (c) Reproduced with permission [145]. ©2017, American Chemical Society.

Typical examples of argyrodite-type sulfides include halogen-tuning argyrodites $\text{Li}_6\text{PS}_5\text{X}$ ($\text{X} = \text{Cl}, \text{Br}, \text{and I}$). As shown in Fig. 7(c), by substituting sulfur with halide in the structure, $\text{Li}_6\text{PS}_5\text{X}$ exhibits a stacking structure with octahedral Li_6S^{5+} and tetrahedral PS_4^{3-} [145]. Moreover, the halide substitution enables the formation of $\text{Li}_6\text{PS}_5\text{X}$ argyrodites with promising ionic conductivity but poor cathode interface stability [156,157]. $\text{Li}_6\text{PS}_5\text{Cl}$ demonstrates a narrower oxidation stability window (2.01 V) compared with the Li_3PS_4 binary system (2.31 V), as shown in Table 2. However, high iodine-containing argyrodite sulfides $\text{Li}_7\text{P}_2\text{S}_8\text{I}$ (LPSI) comprising the substructure Li_6I^{5+} and PS_4^{3-} , shows improved stability over Li_3PS_4 [158]. This improvement is attributed to the generation of an electronically insulating passivation layer that prevents further degradation.

These three types of sulfide electrolytes are all sensitive to the humidity ambient, which triggers serious degradation, inducing crystal structure change, ionic conductivity decrease, and generate toxic H_2S gas. Tatsumisago et al. investigated the degradation mechanisms of $x\text{Li}_2\text{S} \cdot (100-x)\text{P}_2\text{S}_5$ (mol%; $67 \leq x \leq 80$) glasses and $75\text{Li}_2\text{S} \cdot 25\text{P}_2\text{S}_5$ glass-ceramics when exposed to the humidity air [162,163]. Tatsumisago found the generation of H_2S is highly dependent on the glass composition. For example, $75\text{Li}_2\text{S} \cdot 25\text{P}_2\text{S}_5$ that consist of PS_4^{3-} units generate less amount of H_2S , while $67\text{Li}_2\text{S} \cdot 33\text{P}_2\text{S}_5$ consists of $\text{P}_2\text{S}_7^{4-}$ produces more. Therefore, they assumed that PS_4^{3-} unit were harder to hydrolyze than $\text{P}_2\text{S}_7^{4-}$. Liang et al. used the rules of the hard and soft acids and bases (HSAB) theory to explain the stability of the sulfides to humidity [164]. The principle of this theory is that hard acid preferentially reacts with hard base while soft acid is more likely to react with soft base. Based on HSAB theory, the atom P of most sulfides which is a strong acid reacts preferentially with oxygen which is a hard base to form P—O bond, rather than the formation of P—S bond with weak base S.

Several promising approaches, including compositional tuning and morphological control, are the most popular for the electrochemical

stabilization of sulfide-based electrolytes. With the doping of transition metal or oxygen ions, the substitution of cations or anions in the sulfides promotes increased ionic conductivity and chemical stability with the Li metal anode. For the LGPS structure (Fig. 6d), Al^{3+} cation substitutions lead to the LAIPS, with improved interface stability and enhanced cycling stability that allows for an electrochemical window higher than 5.0 V vs. Li [159]. Theoretical calculations related to LGPS structure indicate that Zn^{2+} or Y^{3+} substitution-induced compounds, including LZPS ($\text{Li}_{1+2x}\text{Zn}_{1-x}\text{PS}_4$, $0 \leq x \leq 0.5$) and $\text{Li}_3\text{Y}(\text{PS}_4)_2$, exhibit increased phase, electrochemical, and interface stabilities, while maintaining extremely high room temperature ionic conductivities (Fig. 6e) [160]. In addition to cation substitutions, anion substitution is another feasible approach for improving sulfide electrochemical stability. Zhang et al. reported the development of $\text{Li}_6\text{PS}_{5-x}\text{O}_x\text{Br}$ ($0 \leq x \leq 1$) through O^{2-} doping in $\text{Li}_6\text{PS}_5\text{Br}$ argyrodite [48]. ASSBs based on $\text{Li}_6\text{PS}_{4.7}\text{O}_{0.3}\text{Br}$ sulfide electrolytes deliver high specific capacity, superior rate capability, and outstanding cycling stability accompanied by low interfacial resistivity. $\text{Li}_6\text{PS}_{4.7}\text{O}_{0.3}\text{Br}$ -based ASSBs can function effectively over 900 cycles at a higher current density of 0.4 mA cm^{-2} . However, $\text{Li}_6\text{PS}_5\text{Br}$ can only sustain 560 cycles at a low current density of 0.1 mA cm^{-2} before short-circuiting. Cross-sectional SEM observations reveal many cracks in $\text{Li}_6\text{PS}_5\text{Br}$ after 560 cycles, whereas $\text{Li}_6\text{PS}_{4.7}\text{O}_{0.3}\text{Br}$ after 900 cycles is still intact, indicating excellent dendrite suppression via O doping. Besides the compositional modifications, surface engineering of SSE is also critical for the improvement of electrochemical stabilities. Atomic and molecular layer deposition (ALD & MLD) are promising approaches for SSE surface modifications. The benefits of ALD & MLD technique include, (i) high flexibility for a large variety of SSEs, (ii) feasible process with low temperature and pressure requirements, and (iii) generate large-scale pinhole-free films, which is suitable for scale-up productions. Meng et al. summarized the recent advances of ALD & MLD techniques [165,166].

Regarding the morphological control of sulfide-based electrolytes,

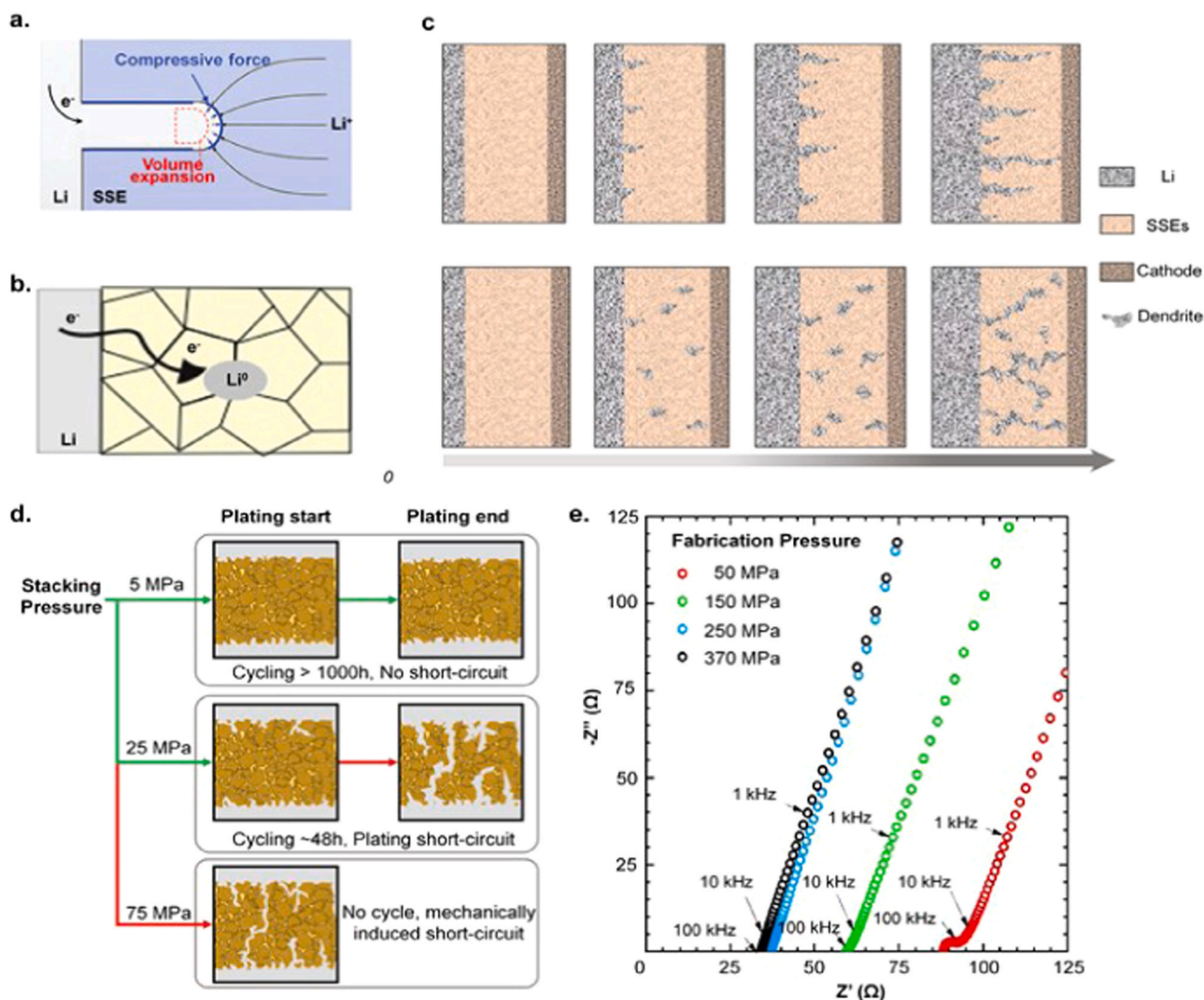


Fig. 8. (a) Nucleation of Li metal on SSE flaws, inducing filament propagation [167]. (b) Filament growth induced by the electronic conductivity of the SSE [171]. (c) Two major filament growth mechanisms. (d) Effect of stack pressure on the short-circuiting of Li metal SSBs [55]. (e) Nyquist diagrams of electrochemical impedance spectra upon various fabrication pressures.

(a) ©2017, Royal Society of Chemistry. (b) ©2019, Nature. (c) Reproduced with permission [170]. ©2019, Nature. (d) ©2020, Elsevier. (e) Reproduced with permission [172]. ©2020, Royal Society of Chemistry.

recent research has focused on improving chemical stability with active materials by broadening the electrochemical window. Li et al. developed a core-shell sulfide electrolyte structure with a crystalline lithium tin phosphorus sulfide ($\text{Li}_{10}\text{SnP}_2\text{S}_{12}$, also referred to as LSPS) core and amorphous shell [161] (Fig. 6f). LSPS sulfides are reported to have a generally narrow stability window of approximately 1.7–2.1 V, while their core-shell structure shows a much wider stability window of 0.7–3.1 V and a quasi-stability window of up to 5 V, with high Si composition in the shell. Theoretical computation reveals that the shell's effective compressibility ensures the pristine structure of LSPS and maintains its ion conductivity during battery cycling, thus enabling a wider electrochemical stability window. In addition to the core-shell structure design, decreased sulfide electrolyte particle size can improve the contact area with the active materials, which is critical to establishing effective ion-conducting pathways and thus improved electrochemical stability.

4.2. Mechanical stability challenges of sulfide electrolytes

4.2.1. Crack-induced Li dendrite formation

The mechanical stability of SSEs is vital for developing commercially successful ASSBs that can operate under harsh operating conditions. Especially for sulfide electrolytes, the brittle mechanical nature (e.g., low fracture toughness) [39] of sulfide composites can worsen pre-existing defects (Griffith flaws) [138] and potentially introduce new flaws upon cycling. Recent efforts have involved comprehensive studies of the mechanical properties of sulfide electrolytes for developing safe and stable ASSBs. Chiang *et al.* reported their study of internal mechanical failure of the glass-ceramic type sulfide electrolyte, $\beta\text{-Li}_3\text{PS}_4$, which found that additional nucleated Li metal on the corner tip of the flaw in SSEs could concentrate the electric field and induce more propagation of the filament (Fig. 8a) [167]. Then, as metal accumulates at the defect space, the electrolyte will reach its stress limit of cracking, resulting in a larger crack with subsequent Li filling [41,168]. Alternating between cracking and Li filling can eventually penetrate the SSE and induce a short-circuit failure. Many *in situ* and *ex situ* tests have

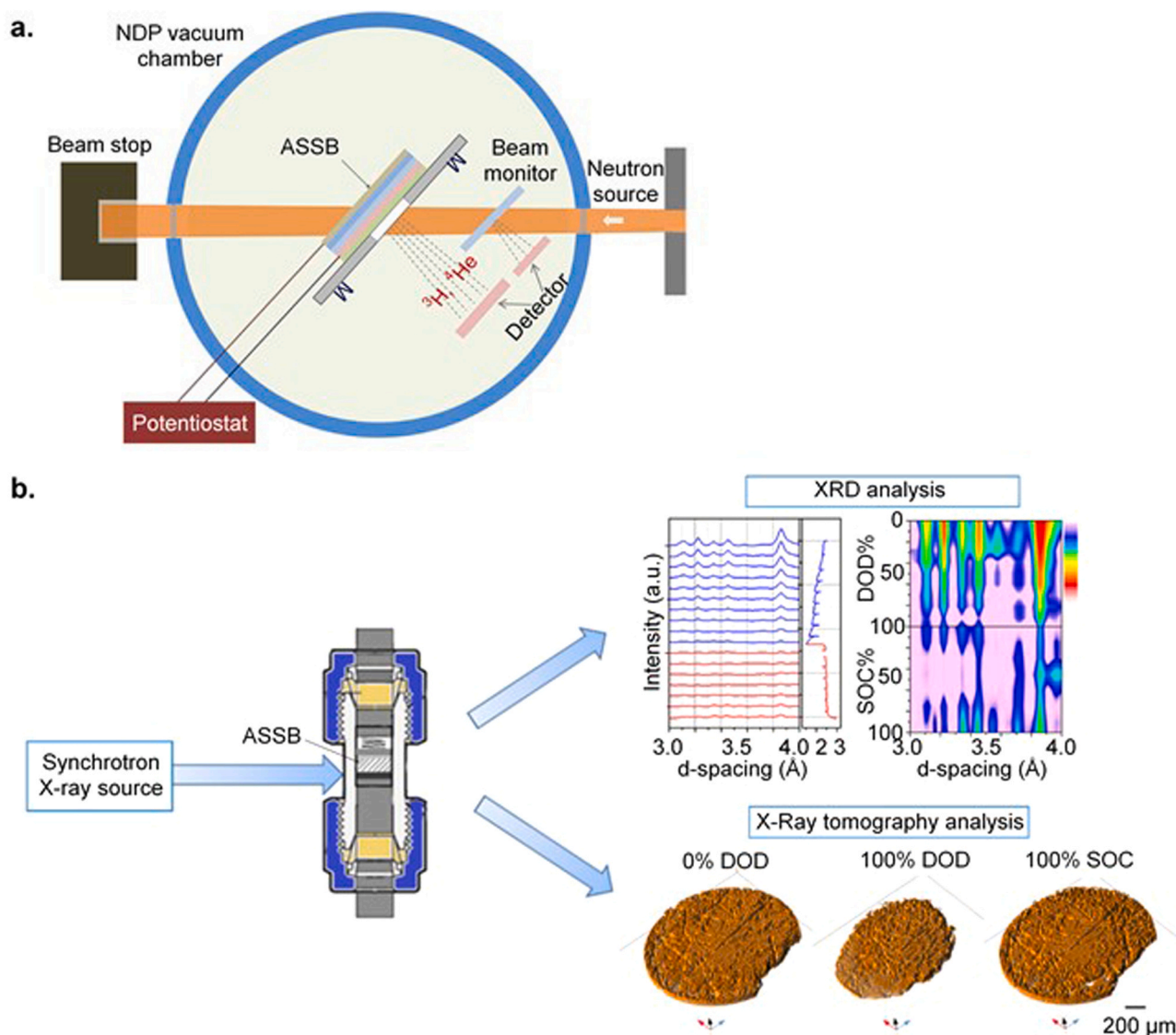


Fig. 9. (a) Experimental schematic of *in situ* neutron depth profiling (NDP) of an ASSB [171]. (b) *In situ* synchrotron X-ray diffraction and tomography setup [176]. (a) ©2019, Nature. (b) ©2020, American Chemical Society.

confirmed the low yield stress of the Li filament generated from the interface penetrates the high shear modulus of SSEs, such as glassy $\text{Li}_2\text{S-P}_2\text{S}_5$ (8.3 GPa) and glass-ceramic $\beta\text{-Li}_3\text{PS}_4$ (8.7 GPa) during cycling [39,169]. Together, these observations indicate interface-driven Li propagation in the presence of sulfide-based electrolytes.

In addition to interface-driven effects, the high electronic conductivity of the SSE may be a predominant factor in filament growth [170, 171] (Fig. 8b). Wang et al. reported that Li metal nucleation grew directly in bulk SSE [171]. Using neutron depth profiling (NDP) of $\text{Li}_2\text{S-P}_2\text{S}_5$ and $\text{Li}_7\text{La}_3\text{Zr}_2\text{O}_{12}$ (LLZO), they also found that Li metal distribution is uniform among the SSE and that Li content increases with plating time. These findings reveal that Li plating occurs at different depths of the SE, rather than gradually developing from the interface. While SSEs with high electronic conductivity facilitate Li ion nucleation, electronic conductivity is responsible for the propagation of metallic Li filaments. This mechanism demonstrates the utility of suppressing filament growth during Li plating by employing SSEs with a lower electronic conductivity and identifying electronic conductivity as a significant criterion for SSE selection. This approach is especially

essential for the build-up of sulfide-based ASSBs resulting from the high electronic conductivity of sulfide composites. Therefore, identifying and addressing properties of the sulfide composite that are responsible for high electronic conductivity will be critical for future research. However, there is lack of consensus regarding the electronic conductivity-induced and interface-driven mechanisms for Li dendrite generation [170] (Fig. 8c). The electrochemically and mechanically unstable Li-SSE interface exhibits kinetics detrimental to filament growth. In another phase, the sulfide composite bulk usually demonstrates high electronic conductivity [42]. As a result, reconciling these two filament growth mechanisms may be achieved using sulfide-based electrolytes.

4.2.2. Structural collapse of the electrolyte layer

Despite filament growth, mechanical stress develops in the SSE due to the volume change upon cycling and induces the mechanical failure of sulfide electrolytes, a scenario especially relevant for crystalline sulfides, which exhibit high shear moduli. The shear modulus of LGPS is predicted to be 7.9 GPa based on theoretical calculations. The Si- and

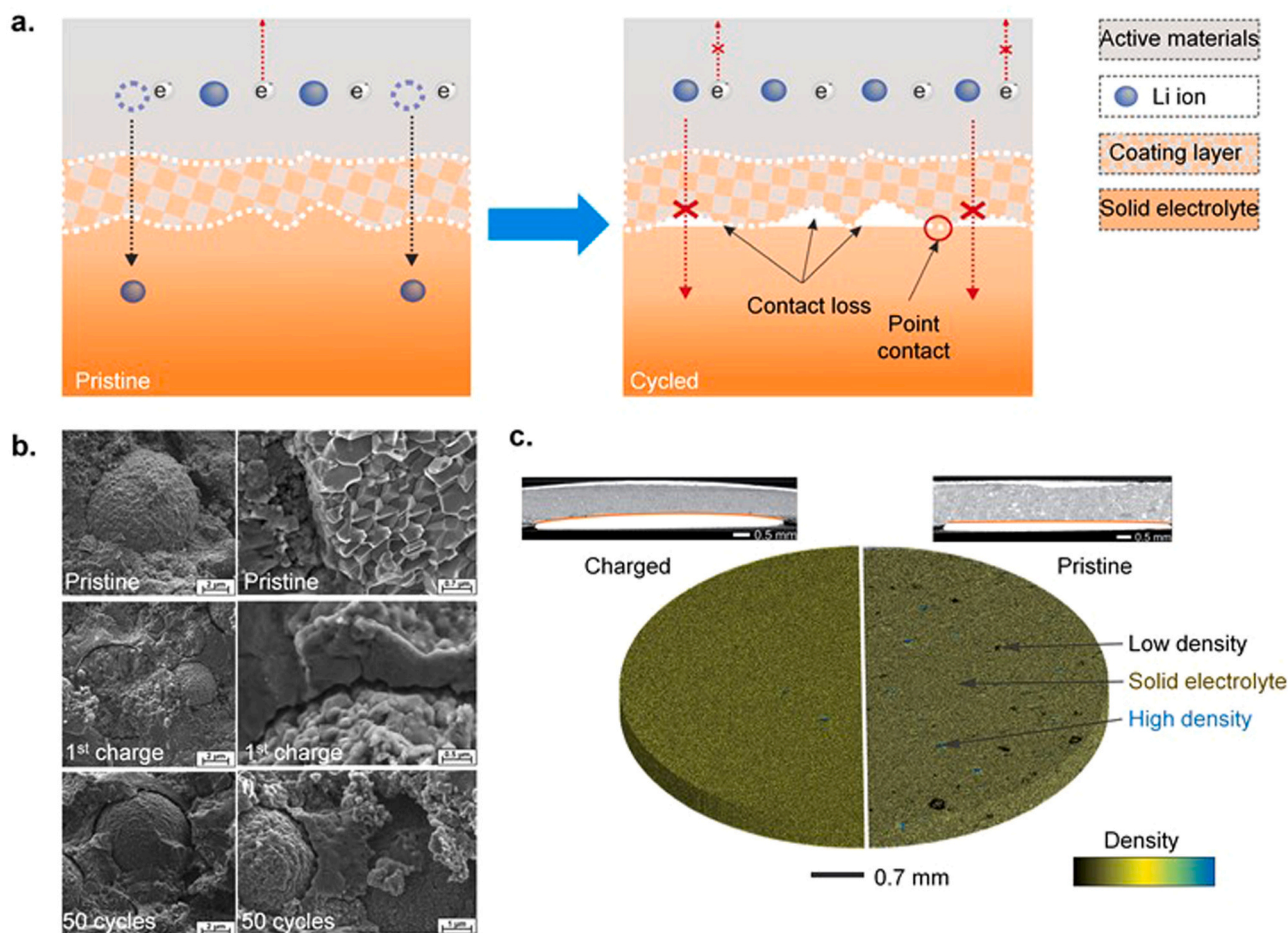


Fig. 10. (a) Contact loss due to volume changes or failures during preparation [180]. (b) The cathode particles shrink during delithiation (charge) and lose contact with the SSE [179]. (c) X-ray tomography of an SSB before and after cycling reveals that significant bending and cracking occur as a result of electrode deformation during electrochemical reactions.

(a) ©2018, American Chemical Society. (b) ©2017, American Chemical Society. (c) Reproduced with permission [175]. ©2017, Royal Society of Chemistry.

Sn-substituted thiophosphates $\text{Li}_{11}\text{Si}_2\text{PS}_{12}$ (LSiPS) and $\text{Li}_{10}\text{SnP}_2\text{S}_{12}$ (LSnPS) are predicted to have higher shear moduli of 9.2 and 11.2 GPa, respectively [173]. A high shear modulus, which is associated with fragility and can amplify intrinsic stress effects on crystalline sulfides, may induce failures more severe than in sulfide glasses with a lower modulus. However, the experimentally measured modulus of LGPS (4.5 GPa) is much smaller than theoretical calculations (7.9 GPa). This discrepancy can be attributed to the reduced van der Waals interactions between the GeS_4 and PS_4 tetrahedra in the synthesized poly-crystalline LGPS that impact its mechanical properties [174]. Therefore, more experimental studies are needed to fundamentally investigate the true nature and impacts of mechanical stress failure related to crystalline sulfides.

Moreover, during cycling, the poor wettability of SSEs results in insufficient contact between the cathode and electrolyte as compared with liquid electrolytes. In general, stack pressure is applied during cell charge-discharge, which is essential for maintain close contact at the anode and cathode interfaces [108]. Meng et al. have studied the influence of applied stack pressure on ASSBs [55,172], as shown in Fig. 8 (d). Their findings indicate that a high stacking pressure (≥ 5 MPa) tends to induce a short circuit and eliminate the porosities inside the electrolyte bulk (Fig. 8e). Many studies have shown that void-free electrode-electrolyte contacts can be implemented through initial high fabrication pressure, rather than maintaining a high pressure, for cell operation [8107,175]. According to this concept, efficient cycling of the ASSB without Li penetration-induced failure is determined by the close

contact created by fabrication pressure, usually in the range of 300–400 MPa. The pressure during cell operation must be high, as the primary function of stacking pressure is to maintain integration of the ASSB by preventing interface delamination induced by the volume change of electrode materials. However, high stack pressure can create new channels for Li propagation or expand pre-existing defects, eventually triggering Li penetration-related failure. Therefore, a lower working stack pressure (≤ 5 MPa) is preferred for long-term stable cycling.

In summary, the potential of using sulfide composites as electrolytes for commercialized ASSBs faces is faced by many challenges, including narrow electrochemical stability windows and mechanical-stress-induced failures, whose resolution is critical for practical applications. Many factors contributing to sulfide electrolyte failure are beneath the surface and usually become more relevant during cycling. To this end, *in situ* techniques are vital for revealing mechanisms of cell break-down that are electrolyte-induced. For example, *in situ* neutron depth profiling (NDP) has been employed to quantitatively analyze dendrite growth [171]. NDP is a non-destructive nuclear analytical technique that can determine the spatial distribution of specific isotopes via neutron capture reactions. Besides, NDP imaging is particularly effective for studying light elements (such as lithium dendrites) in a non-destructive manner. This efficient tool can directly reveal Li distributions during its operation. *In operando* NDP can provide even more information of dynamic Li migration in battery electrodes during operation, as well as the spatial resolution of Li^+ distribution changes. The

experimental setup for *in situ* NDP is shown in Fig. 9(a). Real-time observations using this technique indicate Li dendrites nucleate and grow directly inside the electrolytes. This study also revealed that high electronic conductivities of these materials are responsible for dendrite formation, providing important insight regarding the engineering of SSEs.

In addition to the highly sensitive detection capabilities of *in situ* NDP, synchrotron X-ray tomography (XRT) is another unique non-destructive analytical technique that is valuable for SSB studies. Lemarie et al. have used combined XRT and X-ray diffraction (XRD) to investigate sulfide composites for battery applications [176]; Fig. 9(b) shows the setup and procedures of this approach. The *in-operando* techniques described in this work have revealed much insight into the sulfide-ASSB diagnosis, leading to the successful design of batteries. However, despite advantages of the aforementioned novel *in situ* techniques, their applications in SSEs are not feasible as *ex situ* approaches. To this end, *operando* analysis of SSEs should be encouraged for a better understanding of their (electro)chemical, electrical, and mechanical behaviors. These studies will be critical in elucidating sulfide electrolyte failure mechanisms and paving the way for establishing a combined model that incorporates contact-fracture mechanics, electrochemical stabilities, SSE bulk impurities, and grain boundaries to determine the appropriateness of sulfide composites for SSE applications.

5. Cathode-SSE interface

Chemo-mechanical effects play a significant role at the cathode-SSE interface. Cathode active material (CAM) particles in solid-state composite cathodes are embedded in the SSE, providing pathways for ionic transportation to the active material. The insertion and removal of ions during the charge and discharge process cause a volume change of CAM particles, thus exerting stress on the SSE. Once its stress tolerance threshold is crossed, the SSE develops microcracks along Griffith flaws or generates voids at the interface, which disconnects the cathode from ion-conducting pathways and results in storage capacity fade [167,175, 177–179]. In addition to void generation, interfacial reactions cause increased impedance and reduce the battery's performance [51,178, 179]. Thus, understanding and controlling the chemical and mechanical evolution of interfaces within composite electrodes is essential to build rechargeable ASSBs with long lifetimes. Zhang et al. have described two possible degradation models related to the interface between sulfide-based electrolyte (LGPS) and LiMO_2 CAM (LiCoO_2), including interface contact loss upon CAM volume changes (Fig. 10a) and decomposition of the sulfide-based electrolyte at high voltages [180] (Fig. 11a).

5.1. Contact loss at SSE-CAM interface

Contact loss due to delamination at the cathode-SSE interface significantly deteriorates the battery's electrochemical performance.

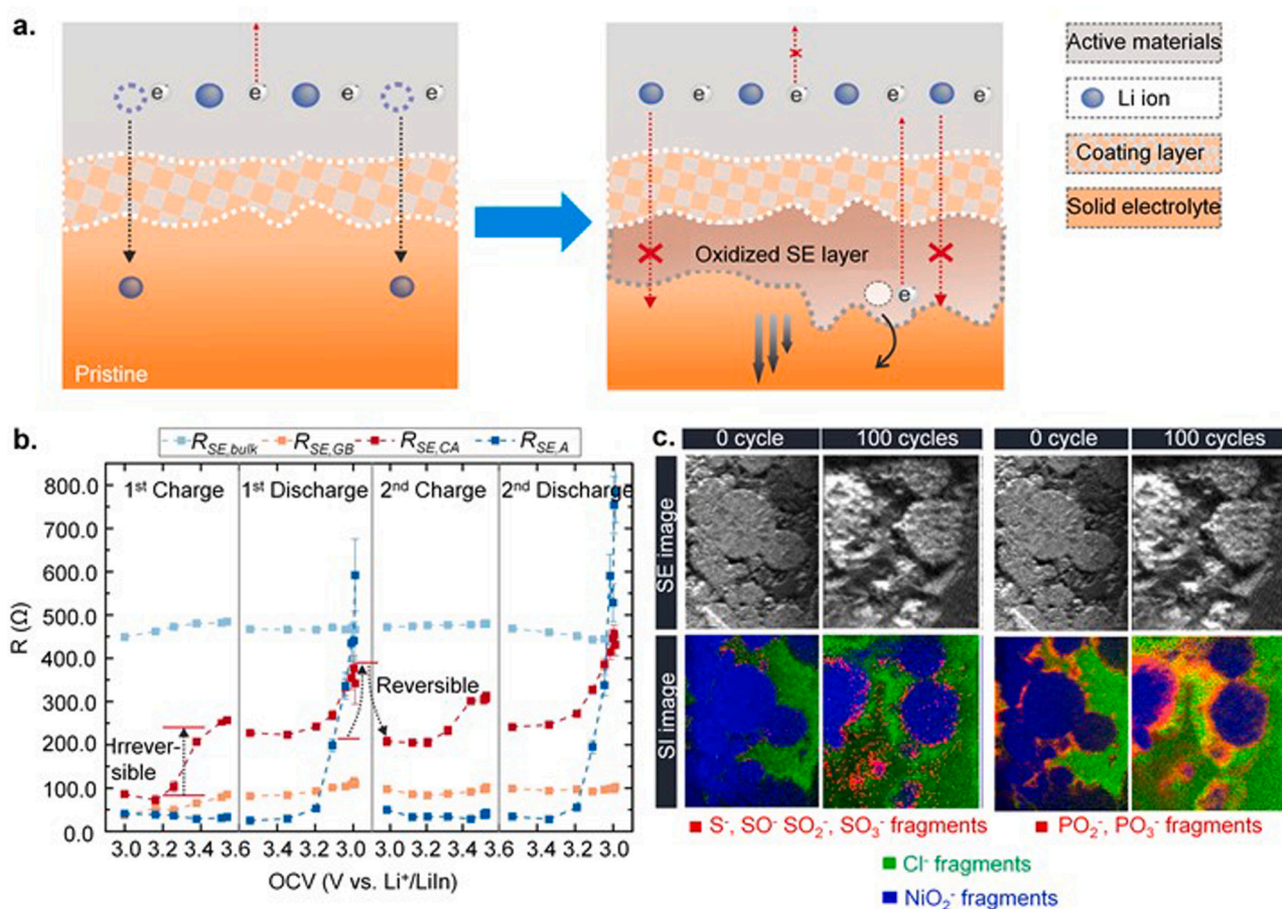


Fig. 11. (a) Li depletion layer formation upon SSE decomposition at high voltages [180]. (b) The SSE-cathode interfacial resistance (red markers) increases irreversibly during the first charge but exhibits reversibility in subsequent cycling, indicating interphase formation [179]. (c) Formation of transition metal fragments during cycling.

(a) ©2018, American Chemical Society. (b) ©2017, American Chemical Society. (c) Reproduced with permission [192]. ©2019, American Chemical Society.

Numerous studies were therefore conducted to understand the chemo-mechanics of composite SSE and resolve the issues [175,181–187]. Among these studies, the fundamental analysis of delamination effects using state-of-the-art techniques has provided valuable information regarding interface stress-strains. Janek *et al.* reported the experimental evaluation of chemo-mechanical degradations at the $\text{Li}_3\text{PS}_4\text{-NMC}_{811}$ cathode interface [179] and directly observed contact loss of the interface during the first cycle (Fig. 10b). Although delamination did not worsen in subsequent cycles, the battery's capacity diminished. Coupling *in situ* observations with electrochemical impedance spectroscopy revealed that early delamination is responsible for isolating CAM particles from the surrounding electrolyte. Breaking of the ion-conducting channel at the SSE-CAMSSE interface results in successive capacity loss.

Novel non-destructive characterization techniques have intrinsic advantages for quantitatively assessing local mechano-structural evolutions with cycling performance. Zhang *et al.* have monitored pressure changes of the LGPS- LiCoO_2 cathode interface through synchrotron XRT [175] to study void generation mechanisms and the compressibility of SSB components (e.g., SSE and composite cathode pellets) upon chemical expansion. They found that the change in compression during the galvanostatic charge-discharge process almost linearly correlates with the charge transfer amount (Fig. 10c). However, their XRT results indicate that significant bending and cracking of the SSE pellet occurs at the pristine and charged stages [177], which can be attributed to electrode deformation due to electrochemical reactions. Moreover, a 3D reconstruction model indicates consolidation of the SSE pellet. Although some amount of volume change clearly fills pores in the SSE, the remaining volume change leads to stress-induced propagation and delamination. To explore the correlation between internal expansion and battery failure, Koerver *et al.* carried out a quantitative analysis of ASSB electrode expansion. They utilized three techniques to investigate the mechanism and implementation of “zero-strain” electrodes [75]:

- 1) *In or ex situ* XRD-based crystallographic volume measurement of a single material as a function of state of charge. The function can be expressed as:

$$\text{Lattice parameter } a, b, c = f(c(\text{Li})) \quad (5.1)$$

In this approach, volume variations were calculated based on Li insertion extraction-induced lattice parameter changes. However, combinatory effects in the composite electrodes (e.g., porosity of the composite electrode, softness and plasticity of SSEs) were not considered.

- 2) Measurement of open-circuit voltage (OCV, E_{oc}) as a function of pressure (p),

$$\left(\frac{\partial E_{oc}}{\partial p}\right)_{T, n_i} = -\frac{1}{nF}\Delta_r V_m \quad (5.2)$$

Here, $\Delta_r V_m$ is the reaction volume, n is the number of transferred electrons, and F is the Faraday constant. The function is established based on external load mechanisms. However, mechanical deformations of the electrode materials were not involved.

- 3) Measurement of pressure change (Δp) as a function of volumetric strain (ε_{vol}), and K is the bulk modulus,

$$\Delta p = -\varepsilon_{vol} \cdot K \quad (5.3)$$

Upon inclusion of plasticity and deformation effects, the stress measurements demonstrate a practical response of the battery. The group also applied several approaches for addressing stress-induced strain during battery cycling, including the use of zero-strain electrode materials and compensating for large-volume expansion materials (e.g., NMC) with large-shrinkage electrode materials (e.g., LiCoO_2) in the composite electrode. Findings from this analysis are discussed

extensively in the following section.

Beyond electrode volume changes, critical particle sizes based on cathode volume changes can be considered and tweaked for specific ASSBs [188]. Based on a study conducted by Wang *et al.*, silicon nanoparticles may be used for homogenous stress distribution and to lower the mean bulk modulus of the cathode to better distribute the stress and prevent plastic deformation [189]. Considering that harder cathode materials increase the composite's elasticity modulus, the researchers added flexible binders to prevent cracks. In a related study, Oh *et al.* proposed a single-step, sheet-type cathode fabrication approach for incorporating polymeric binders (nitrile-butadiene rubber [NBR] or polyvinyl chloride [PVC]) in the $\text{Li}_3\text{PS}_4\text{-NMC}_{622}$ composite cathode [64]. A developed thin-film ASSB assembled with a thin-sheet cathode shows a high reversible capacity, which is attributed to the binder in the cathode that is reducing local stress and thus preventing the delamination and cracks. In addition, Rosero-Navarro *et al.* used wet processing to incorporate ethyl cellulose as a binder in the $\text{Li}_6\text{PS}_5\text{Cl-NMC}_{111}$ composite cathode to enhance electrochemical performance [190]. A high-capacity retention rate of 91.7% after 10 cycles was obtained with binder-mixed composite cathodes. Moreover, they quantitatively evaluated the impacts of binder amount on the battery's overall electrochemical performance and found that a binder content greater than 1% w/w led to capacity loss due to insufficient ion-conducting channels in the composite cathode. However, a lower binder content (e.g., 0.5% w/w) will not hinder electrochemical performance but instead increase elasticity of the electrolyte and composite cathode. The aforementioned binder-based wet solutions aid in processing and production of ultra-thin electrolyte and composite cathode sheets, enabling batch-fabrication of high-volume-capacity ASSBs that are preferred by the industry. Despite these binder-related solutions to resolve mechanical challenges on the cathode interface, the engineering of active material particles to address dimension and ratio effects, volume expand-shrink phenomena, and pulverization-disintegration behaviors are also practical approaches to achieve the desired effect.

5.2. Oxidative reactions at SSE-CAM interface

The SSE-CAM interface is the gateway for ions and electrons to access the active material. Therefore, investigating the interfacial reactions that lead to interphase generation for maintaining ion and electron flow to and from the active material is important. Many studies have revealed that during the very first charge, an interphase layer is generated between the cathode and electrolyte due to electrolyte decomposition. In the case of composite cathodes with sulfide electrolytes, the interphase layers are subjected to mechanical, chemical, and electrochemical instabilities. Further chemical-electrochemical degradation of the electrolyte accompanied with microcracks, defects, or structural mismatches are inevitable and detrimental for battery performance [43,60,178,179,191].

As introduced previously, Janek *et al.* conducted *in situ* electrochemical impedance spectroscopy and X-ray photoemission spectroscopy to monitor this formation [179]. *In situ* impedance spectroscopy (Fig. 11b) showed the presence of an irreversible interface formed between NMC_{811} and Li_3PS_4 , while XPS data revealed that interphase formation occurred rapidly during the first charge and continued to grow gradually with successive cycles. Similar degradation was observed in the ASSB with LiCoO_2 and LGPS composite cathodes, wherein the interphase gradually grew thicker with an increasing number of cycles, and battery capacity deteriorated [180,193]. In this work, multiple characterization methods, including STEM, EELS, XRD, and XPS, were combined to probe underlying degradation mechanisms based on two important predictions for reliable interphases: 1) zero-strain materials in the cathode are necessary for mitigating mechanical damages and 2) SSEs with larger electrochemical stability windows are important for creating a stable interface. Despite engineering the intrinsic properties of active materials, the coating layer of

existing popular active materials, such as LiCoO₂ and NMC, show excellent potential for interface stability. While studying the Li₃PS₄-LiCoO₂ interface [191], Sakuda et al. found that S, P, and Co diffused between the SSE and LiCoO₂, implying that side reactions at the interface induce battery deterioration. They proposed the application of a Li₂SiO₃ coating layer on the LiCoO₂ to suppress these side reactions, thus preventing the formation of the interfacial layer. After this pioneering work, researchers adopted various oxide materials, such as LiAlO₂, Li₂SiO₃, LiNb_{0.5}Ta_{0.5}O₃, Li₄Ti₅O₁₂, and LiNbO₃, as a thin-layer coating source to limit cathode interface degradation [43,45,178,180,191,194–197]. Although this solution cannot completely inhibit interfacial reactions, it has successfully maintained low reaction rates and delayed battery degradation. Based on studies related to cathode coating, Zhang et al. have categorized the contact situation between the cathode-coating material and SSE into three cases [180]: (1) an ideal situation in which the cathode particles are well-coated, maintain coating during cycling, and possess high ionic and electronic conductivity. Additionally, the coat has good contact with the SSE, allowing Li ions to transfer reversibly between the cathode and SSE. (2) In a less desirable situation, the coated cathode material is disconnected from the SSE, either due to delamination or a heterogeneous cathode composite mixture. The detachment renders the cathode capacity redundant, as it is out of reach from Li ions and electrons. (3) In the third situation, the SSE has a low electrochemical stability window, causing it to decompose at high voltages. This decomposition leads to Li layer depletion and formation at the interface and a subsequent increase in internal resistance. The Li layer progressively grows, obstructing Li ion movement and causing additional capacity loss.

In a recent study, Walther et al. probed interfacial structural and chemical evolutions with state-of-the-art time-of-flight secondary-ion mass spectrometry (ToF-SIMS) techniques [192] (Fig. 11c), an ultra-sensitive surface analytical technique that provides detailed elemental and molecular information with high lateral and in-depth resolution. Before application of ToF-SIMS, they identified signal changes of S 2p, P 2p, and O 1 s during battery cycling by using XPS on the SSE (Li₆PS₅Cl), which found that potential species distribution changes occur upon interphase formation. However, XPS does not yield conclusive data due to a lack of information obtained regarding the intermediate states of transition metals involved with interfacial reactions. When combined, XPS with ToF-SIMS results revealed that transition metal phosphates [e.g., Ni₃(PO₄)₂ and Mn₃(PO₄)₂] emerged upon interphase formation [198]. In addition to transition metal phosphates, transition metal sulfates were also detected at the interface through ToF-SIMS depth profiling. Increased signals of both transition metal sulfates and phosphates at the interface after battery cycling indicated that interface formation is primarily affected by sulfate and phosphate. Besides the interfacial reaction, the space charge layer (SCL) and the chemical bond vibration also bring negative effects. Zhang et al. reveals the generation of SCL between sulfide electrolytes and high capacity cathodes (e.g. nickel-rich layered oxides) during the cycling. The SCL significantly affect the internal resistance and become long-term battery degradation mechanism [199].

Based on these studies on the cathode interface, maintaining optimum functioning of the interface is vital for the battery's performance and capacity. The interface is mainly affected by the generation of voids and interfacial reactions. Voids often reduce the contact area, causing more constricted pathways and leaving some amount of active material inaccessible for energy storage. Reactions involved in interface formation hampers ionic transportation, induce morphological changes that cause delamination, and in extreme cases, block ion exchange between the SSE and CAM. In ASSBs, the SSE-CAM interface is responsible for approximately 30% of the capacity that is lost during the very first cycle. Thus, preventing this decay would significantly boost the battery's life, highlighting the importance of conducting more in-depth studies to better understand the fine details of this interface and enhance battery performance.

6. CAM challenges

In ASSBs, CAMs determine cell energy density through its voltage and potentials [9,10,12]. CAM particles are mixed with the SSE to form a composite cathode [10,178]. As discussed above, poor compatibility between CAMs and sulfide electrolytes cause multiple issues such as interfacial contact loss and reductive interfacial reactions. However, CAM particles are also involved with chemo-mechanical challenges induced at a high operating voltage. Layered LiMO₂ cathodes (M = Ni, Mn, Co: NMC; M = Ni, Co, Al: NCA) are the most often investigated CAMs for high-energy-density batteries [12]. In particular, ternary transition metal oxides with general formulas LiNi_xMn_yCo_{1-x-y}O₂ (NMC) and LiNi_xCo_yAl_{1-x-y}O₂ (NCA) enable a high working voltage and high-volumetric specific energy and have shown great potential for EV applications [13,200–204]. However, LiMO₂ ternary cathode materials suffer from chemo-mechanical degradation, including irreversible capacity decay, voltage drop, and reduced cycling life [9,204–206], due to point defects, particle cracks and disintegration. In this section, we will summarize the experimental evidence provided for high-voltage LiMO₂ ternary cathode materials performance, degradation mechanisms (including size and ratio effects), volume expansion-shrinking phenomena, and pulverization-disintegration.

6.1. Size and ratio effects

Recent experimental studies on NMC and NCA cathodes show the relation between particle dimensions and ratios and battery performance [178,188,207]. Strauss et al. reported that NMC particle size could impact ASSB capacity [188] and demonstrated that decreasing particle size ($d \ll 10 \mu\text{m}$) improved the battery's specific capacity. Smaller particles allow more contact points at the cathode interface, providing better ionic percolation pathways. As the average particle size of the NMC in their study is much smaller than 10 μm , near-full capacity in the first charge cycle was achieved (Fig. 12a). They also determined the ratio effect of composite particles according to desired purposes. For high-energy-density battery applications, more particles are needed in the composite cathode, which enables higher electronic conductivity by limiting ionic transport. In contrast, more SSE and fewer NMC particles in the composite cathode allow better ionic conductivity suitable for these batteries. Thus, an optimal size ratio between NMC particles and the SSE in the cathode is critical for creating a mixed percolation network for optimized ionic transport and mitigating electronic resistance. Moreover, as ASSBs are generally featured with high-mass loading of NMC particles [9,10,12], the interparticle interface ratio represents ionic-electronic percolation network conditions in the composite cathode in various contexts [118,208,209]. For example, a higher ratio of the interparticle interface in the composite cathode indicates less effective ionic paths [12], whereas a lower ratio is suggestive of reduced mutual contact between particles and the completeness of the SSE percolation network. These results clearly demonstrate that a higher interparticle interface ratio is suitable for high-energy batteries, while a lower rate is more appropriate for high-power applications [188].

6.2. Volume expansion-shrinking phenomenon

In composite cathodes blended with sulfide SSEs and CAMs, although sulfide electrolytes are relatively softer than oxide-based electrodes, mismatch problems still occur in the cathode interphase. The selection of porous electrolytes can partially address these issues in the cathode interfaces [210], but a significant volume change of NMC or NCA particles during charge-discharge still leads to contact loss and electrolyte cracks [75,211]. Generally, the volume of LiCoO₂ particles increases during lithiation and decreases upon delithiation [212], which is referred to as positive volume expansion. In the layered structure of LiCoO₂, cobalt is coordinated octahedrally by oxygen, which provides CoO₆ with edge-sharing layers between which the Li ion intercalates.

During the deintercalation of Li ions, as the amount of positive charge decreases, the negatively charged CoO_6 layers undergo repulsion that pushes the lattice apart [212–214], and a 2% increase in the volume along the unit cell's c-axis can be observed [212]. As a result, pressure increases during deintercalation. Conversely, lithiation causes a decrease in pressure due to reduced repulsion of the negatively charged CoO_6 layers. This phenomenon of changes in lattice volume occurs in various oxide electrode materials and is not restricted to LiCoO_2 [182].

Although NMC is chemically similar to LiCoO_2 , it behaves quite differently during cycling. The layered compounds, such as LiCoO_2 , expand in the z-direction because of the high coulombic efficiency of metal-oxygen layers. However, expansion in the x-y-directions is dependent on the size and nature of transition metals, such as Ni in NMC [181,182,184,215–217]. Unlike LiCoO_2 , NMC behaves more predictably, as its volume decreases during delithiation and increases during lithiation [212]. Volume changes of NMC are reversible but do not exhibit a linear correlation with and intercalation [181,212,218–220], as the expansion and contraction of the lattice are not typically isotropic. Moreover, Ni-rich NMCs tend to undergo significant volume changes, leading to larger voids and more severe delamination between SSEs and cathode layers, primarily due to the significant change in Ni's ionic radius during transition metal oxidation [75]. Thus, cathodes with a lower Ni content (e.g., $\text{LiNi}_{0.33}\text{Co}_{0.33}\text{Mn}_{0.33}\text{O}_2$, and NMC_{111}) will induce fewer voids than high-Ni cathodes (e.g., $\text{LiNi}_{0.8}\text{Co}_{0.1}\text{Mn}_{0.1}\text{O}_2$, and NMC_{811}) [181,184,218–220]. However, reducing the amount of Ni in the cathode is not an ideal solution to address the volume-change-induced challenge faced with composite cathodes [22], as the reduced Ni content in NMCs is associated with a lower specific capacity. Koerver et al. reported the blending of positive volume

expansion of LiCoO_2 and negative volume expansion of NMC in the composite cathode to enable only minimal volume expansion during cycling, while retaining a high specific capacity [75]. Their study has experimentally demonstrate that by cycling a battery with an active material composite of NMC and LiCoO_2 in a weight % ratio of 55:45, respectively, LiCoO_2 shows positive nominal stress, while NMC_{811} shows a negative nominal stress change during the deintercalation phase of the cycle. Fig. 12(b) shows the superimposed stress measurements of cathodes with mixed CAMs (LiCoO_2 and NMC_{811}), which yield a significantly smaller amplitude than those found with LiCoO_2 or NMC_{811} independently. Furthermore, this approach has successfully achieved lower delamination due to changes in volume, providing good contact with ionic conduction pathways after cycling.

In liquid batteries, NMC and NCA demonstrate significant volume changes [200,221–223]. Unlike dynamic mechanisms in the liquid electrolyte, the solid-solid interactions in ASSBs can result in the mechanical failure [224–226]. In the case of composite cathodes, the blending of TCM particles in a sulfide electrolyte creates a large specific surface area similar to that of liquid electrolytes, thus facilitating more ion-electron pathways than with garnet-based electrolytes. However, unlike liquid electrolytes, SSEs can potentially generate point defects, cracks, and structural mismatches at both the particle and electrolyte interface, despite intimate contact. Generally, mechanical impacts on volume expansion-shrink can break stable SEI, exposing the internal active materials and causing formation of a high-impedance interface. Microcracks on the particle will be propagated upon cycling, eventually inducing particle pulverization [227]. Therefore, maintaining smaller volume changes within the composite cathode generates less stress at cathode interfaces and is key to addressing the mechanical and

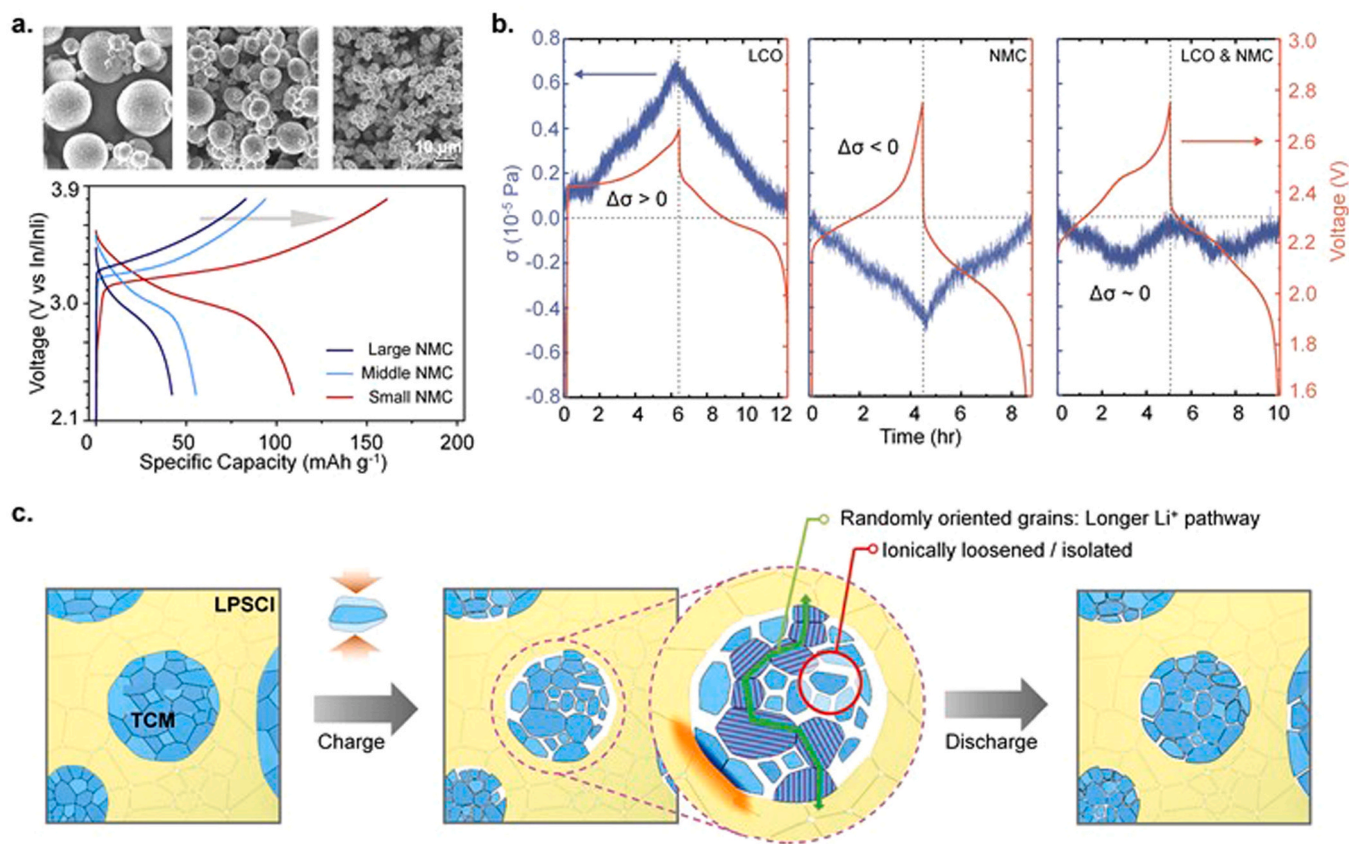


Fig. 12. (a) Dimension and ratio effects on CAM particles and battery performance [188]. (b) Stress mitigation by CAM particle balancing (NMC and LiCoO_2 , 55:45) [75]. (c) Microstructural evolution of the grain boundary on TCMs [224].

(a) ©2018, American Chemical Society. (b) ©2018, Royal Society of Chemistry. (c) ©2020, Elsevier.

chemo-mechanical instability issues associated with composite cathodes.

6.3. Particle pulverization (disintegration)

Much experimental evidence has confirmed structural collapse upon volume changes. Dahn et al. reported the initiation of microcracks on NMCs induced by the ion intercalation-extraction process upon cycling [200,226,227]. They also found that the lattice distance on NMC₁₁₁ (LiNi_{0.33}Mn_{0.33}Co_{0.33}O₂) changes as a function of the charge-discharge voltage. For example, the c-axis lattice was reduced dramatically when over-charged to above 4.0 V, which was attributed to the extraction of Li ions from the layered structure of NMC [200]. In fact, charge-induced CAM lattice collapse is a universal phenomenon associated with Li transportation [224,228] that causes point defects or microcracks. Upon further propagation of these structural defects, overall collapse of the CAM occurs. Sun et al. reported that electrochemical-mechanical effects on randomly oriented primary particles results in internal grain boundary disruption and eventual disintegration of the secondary particle [224]. As shown in Fig. 12(c), the microstructural evolution of the TCM grain boundary is responsible for the poor electrochemical performance of ASSBs as compared with

conventional liquid electrolyte-based LIBs. In ASSBs, the SSE cannot access and wet the internal grains during the evolution and therefore is unable to control the particles' mechanical integrity.

Several approaches to modify the high-voltage mechanical impacts on LiMO₂ CAM particles have been proposed. First, ionic conductive polymers are used in the surface coating of particles [229–231], which serves as a buffer layer to protect the particle from mechanical impacts that reduce potential structural collapse and hence prevent capacity fade. Moreover, inorganic metal oxide coating techniques, such as those using Li₃PO₄ [231–233], have yielded excellent capacity retention at a high cut-off voltage. Manthiram et al. reported that, when combined with an electronically conductive polypyrrole (PPy) [233], unfavorable defects of Li₃PO₄ coating can be addressed (Fig. 13a). In addition, high-elasticity PPy can alleviate the impact of internal stress on the particle, preventing crack generation. Second, CAM particles with mutually reinforced chemo-mechanical properties (e.g., NMC and LiCoO₂) can be mixed to balance the strain on the overall cathode composites to enhance capacity retention and voltage stability. This strategy can be extended to the tailoring of battery component selection for the design of a solid-state cell. Different combinations of battery components, including the electrode, SSE, and separator, can lead to distinct chemo-mechanical properties for the desired applications.

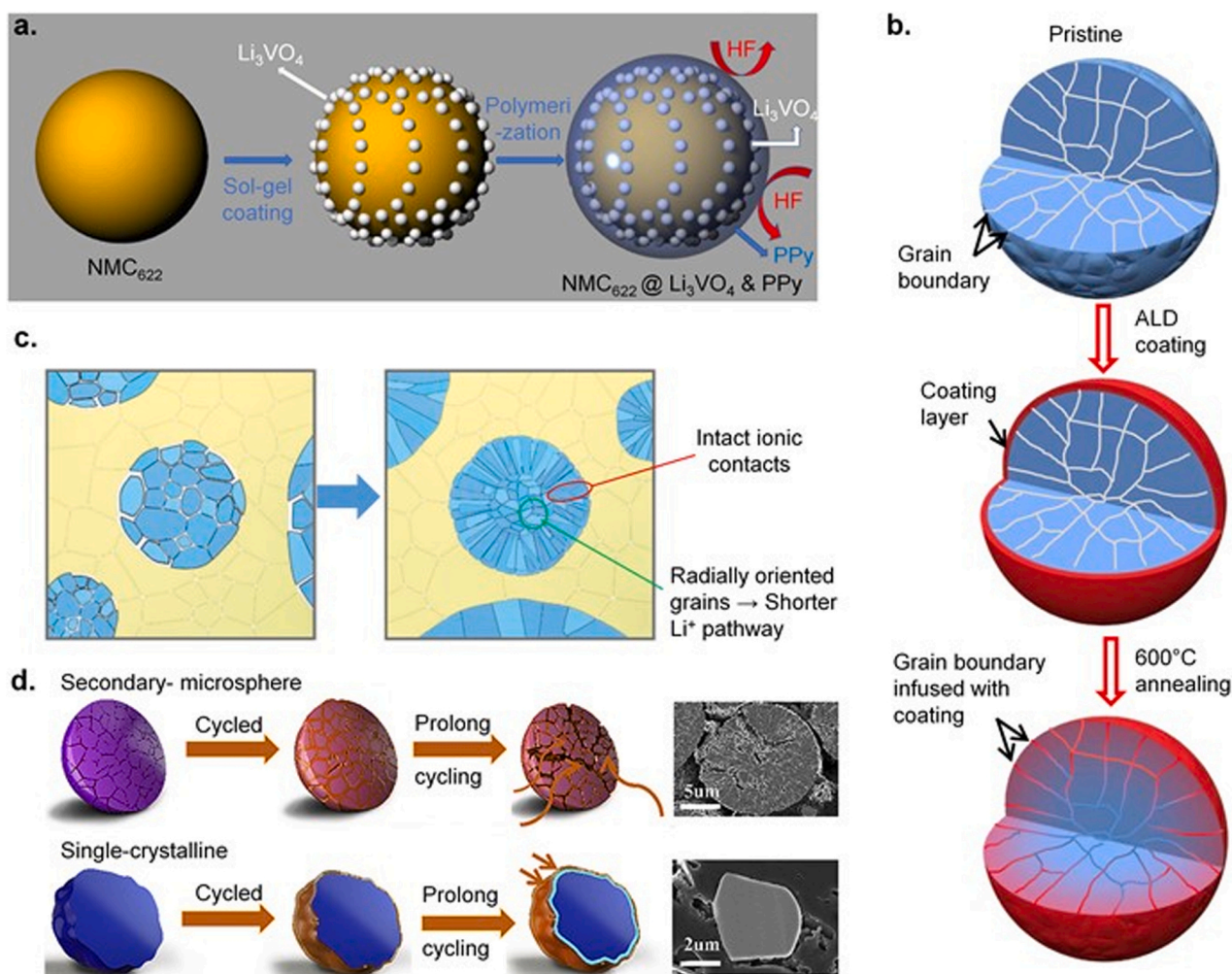


Fig. 13. Approaches of mitigating mechanical impacts on TCMs. (a) Internal stress impact alleviated by a high-elasticity polypyrrole (PPy) [233]. (b) Capacity retention and voltage stability enabled by intergranular coating [234]. (c) Radially oriented secondary particle architecture allows long-term cycling stability in ASSBs [224]. (d) Improved structural stability and cycling performance realized by a single crack-free, crystalline CAM particle [235].

(a) ©2017, American Chemical Society. (b) ©2018, Nature. (c, d) ©2020, Elsevier.

Regarding microstructural stability of the secondary LiMO_2 CAM particles (Fig. 13b), achieving intergranular coating into the grain boundaries of the particle is essential for enhancing capacity retention and voltage stability without suffering failure (e.g., disintegration) caused by anisotropic volume changes [234]. Third, architectural manipulations of CAM microstructures can potentially address the discussed mechanical challenges. Fig. 13(c) shows that a radially oriented secondary particle architecture can accommodate volume changes without causing mechanical degradation and exhibits much better long-term cycling stability in sulfide ASSBs than do particles with randomly oriented architectures [224]. Moreover, using a crack-free, single crystalline CAM particle improves structural stability and cycling performance (Fig. 13d) [235]; Yang et al. has summarized the critical role of the CAM microstructures to the stability and capacity performance of the ASSB [236]. The single crystal NMC_{811} with good mechanical integrity breaks the electrochemical performance limit of the conventional polycrystalline NMC_{811} in the ASSBs. Finally, many alternative CAMs with excellent electrochemical performances and optimized mechanical properties are emerging. In recent years, organic cathode materials (OCMs) have shown advantages as well, such as a high energy density, cost effectiveness, being environmentally friendly, and easily modifiable, compared with their inorganic counterparts [15,237]. Some newer studies have revealed that combinations of OCMs and sulfide SSEs are desirable for specific energy and cycling stability, which are beneficial for high-energy applications, such as hybrid EVs, and smart grids. Compared with CAMs, OCMs possess favorable structural properties related to sulfide electrolytes that can prevent volume change-induced mechanical stress and corresponding crack formation on the interfaces. Thus, a more in-depth understanding of ion-electron transport mechanisms can maximize the value of OCMs in practical battery cathode solutions aimed at achieving high-performance sulfide Li metal batteries.

7. Summary and outlook

This review focuses on the practical challenges related to battery architecture comprising a Li metal anode, sulfide electrolyte, and Ni-rich layered oxide cathode. ASSBs based on such architecture show great promise in high energy-power applications (e.g., EVs) due to their high energy density, safety, and broad range of operating temperatures. However, many barriers exist regarding our understanding and control of these components' intrinsic instabilities, as well as the structural-chemical-mechanical evolutions of the Li anode, sulfide-based SSE, Ni-rich cathode, Li-SSE anode interface, and SSE- LiMO_2 cathode interface. Our discussion here highlights recent discoveries of the material properties of each battery component and their interplay during electrochemical cycling. For example, the coupling effects of Li metal creep and contact elastoplasticity in the Li anode can result in insufficient physical contact and uneven current distributions between the electrolyte, which eventually induces the formation of metal filaments and interfacial porosities. Second, high impedance originates from the interphase between the Li metal anode and sulfide electrolyte due to interfacial reactions. In addition, mechanical failures induced by dendrite penetration compromise interphase stabilities. Third, narrow intrinsic thermodynamic/electrochemical windows are a shortcoming of sulfide electrolytes regarding electrolyte degradation during cycling, and the soft nature of the sulfide electrolyte should also be considered in the design of ASSBs. Fourth, interactions between the sulfide electrolyte and high-voltage cathode cause significant chemo-mechanical degradation, such as contact loss and a Li-depleted, high-resistance interphase. Fifth, dimension and ratio effects, substantial volume changes, and the pulverization-disintegration of cathode particles during cycling can exacerbate structural defects and cause collapse. These explorations provide fundamental insight into the understanding and prediction of Li-SSE- LiMO_2 battery behaviors. However, more research is needed to address the technical challenges related to materials, electrodes,

electrolytes, and battery designs for improved engineering of Li-SSE- LiMO_2 -based ASSBs. Perspectives for future investigations are outlined below.

7.1. Stable interfaces between the electrolyte and electrode

The formation of a stable ion-conductive and electron-insulative interface between the electrolyte and electrode is critical for controlling chemo-mechanical reactions. Lee et al. from Samsung reported an anode free ASSB setup with silver-carbon (Ag/C) interlayer regulated Li deposition effectively [238]. Carbon plays the role of a separator to keep the SSE layer away from Li metal. This enhances the durability of SSE and prevents the penetration of Li metal through the SSE, due to their strong modulus of ~ 200 GPa. To achieve uniform Li deposition, Ag was applied to lower the nucleation energy of Li metal by forming Ag-Li alloy. Wang et al. coated a cold-pressed $\text{Li}_3\text{N-LiF}$ composite on LPS electrolyte to promote Li dendrite-suppression capability [239]. LiF with high interface energy can enhance nucleation energy and inhibit Li dendrite penetration, while Li_3N enabled high ion conductivity can reduce Li plating/stripping overpotential. Moreover, the pores in the composite adjacent to Li metal serve as Li reservoirs enhanced the interfacial contact. The coated electrolyte achieved a high CCD of $> 6 \text{ mA cm}^{-2}$ and 6 mAh cm^{-2} capacity at room temperature. For the cathode interface, coating with a "buffer layer" material is an effective way to improve the interfacial stability. Yang et al. succeed in achieving a nanoscale solid solution surface layer containing Ti on the active material based on a one step pre-coating method, resulting in an ultra-stable reversible capacity for the battery operations [240]. Li et al. proposed LiNbO_3 coating with about 1 wt% content is adopted to improve the interfacial stability and the electrochemical performances of NMC_{811} cathode in solid-state battery using $\text{Li}_{10}\text{GeP}_2\text{S}_{12}$ solid electrolyte [241].

Future work should also aim to design new sulfide electrolytes with wider potential windows (e.g., doping of halide elements) and materials engineered for higher volume change tolerance by including artificial buffer layers to prevent electrolyte decomposition and to suppress dendritic growth. Considering these factors are critically important for improving the electrochemical performance of ASSBs related to rate capability, energy-power density, and cycle life.

7.2. Thin-layer ASSBs fabrication

Typical lab-produced ASSBs are based on press-formed dry mixing electrolyte-cathode sheets and thus suffer from limited scalability. The slurry coating process involving the binder can offer adhesion between electrolyte materials and ionic conductivity comparable to that of the dry mixing-based counterpart [242]. This solution-based casting process can be adopted to cathode sheets to facilitate the homogeneous dispersion of active material particles in the slurry and the as-formed composite cathode layer. The solution-processed electrolyte and thin-layer cathode can likely exhibit decent performance with respect to rate capability and cyclability due to the high homogeneity of the electrode-electrolyte components. A continuous wet coating process, such as roll-to-roll, is suitable for high throughput of ASSB layer formation. However, mechanical properties of the components, including adhesiveness, bending stiffness, and elastic-plastic features, should be considered during manufacturing and processing. Sulfide-based SSE membranes with high ionic conductivity, fabricated by adding small amount of binders, are promising for roll-to-roll manufacturing. Furthermore, the production environment is also critical to the battery's success due to the negative effects of highly reactive sulfide composites; thus, an inert or dry atmosphere should be considered for thin-layer ASSB batch fabrication.

7.3. *In situ/operando* diagnosis

In situ/operando diagnosis can provide first-hand, in-depth information of the ASSB under operation conditions. Unfortunately, the buried electrode, interface, and electrolyte limit the direct characterization of potential morphological-chemical-mechanical evolutions. Thus, non-destructive techniques, including NDP, XRT, and acoustic detection, are encouraged for *in situ* battery analysis. However, current non-destructive tests are favorable for detecting elemental-chemical distributions but not for probing chemo-mechanical and morphological mechanisms. To identify the key structural-mechanical-chemical features beneath the battery's surface, an "open-cell" setup with an intricate cross-section of the ASSB is suggested for performing *in situ* characterization. This setup enables multi-pronged, real-time detection at the interfaces, providing up-to-date information about morphological changes, chemical composition, mechanical properties, and evolutions of electrolyte decomposition products, including intermediate products that may induce negative effects during battery operation.

Declaration of Competing Interest

Y.Y. and Y.L. have equity interest in LiBeyond LLC. Their relationship with LiBeyond LLC has been reviewed and approved by the University of Houston in accordance with its conflict of interest policies. Z.F. has interest in Multi-Diagnosis LLC. His relationship with Multi-Diagnosis LLC has been reviewed and approved by the University of Houston in accordance with its conflict of interest policies.

Acknowledgments

This work was supported by the U.S. Department of Energy's Office of Energy Efficiency and Renewable Energy (EERE) under the Vehicle Technologies Program under Contact DE-EE0008864. Jiatao Lou and Jun Zhang acknowledge the support from National Natural Science Foundation of China under grant Nos. 21972127 and U20A20253.

References

- [1] (<https://www.energy.gov/eere/articles/battery500-progress-update>). (2020).
- [2] R. Van Noorden, *Nature* 507 (2014) 26–28.
- [3] R. Schmich, R. Wagner, G. Horpel, T. Placke, M. Winter, *Nat. Energy* 3 (2018) 267–278.
- [4] H. Li, *Joule* 3 (2019) 911–914.
- [5] F.X. Wu, J. Maier, Y. Yu, *Chem. Soc. Rev.* 49 (2020) 1569–1614.
- [6] K.B. Hatzell, X.C. Chen, C.L. Cobb, N.P. Dasgupta, M.B. Dixit, L.E. Marbella, M. T. McDowell, P.P. Mukherjee, A. Verma, V. Viswanathan, A.S. Westover, W. G. Zeier, *ACS Energy Lett.* 5 (2020) 922–934.
- [7] P. Albertus, S. Babinec, S. Litzelman, A. Newman, *Nat. Energy* 3 (2018) 16–21.
- [8] T. Krauskopf, H. Hartmann, W.G. Zeier, J. Janek, *ACS Appl. Mater. Interfaces* 11 (2019) 14463–14477.
- [9] S. Zhang, J. Ma, Z.L. Hu, G.L. Cui, L.Q. Chen, *Chem. Mater.* 31 (2019) 6033–6065.
- [10] J.H. Yan, X.B. Liu, B.Y. Li, *RSC Adv.* 4 (2014) 63268–63284.
- [11] C.X. Tian, F. Lin, M.M. Doeff, *Acc. Chem. Res.* 51 (2018) 89–96.
- [12] P. Rozier, J.M. Tarascon, *J. Electrochem. Soc.* 162 (2015) A2490–A2499.
- [13] S. Hwang, S.M. Kim, S.M. Bak, K.Y. Chung, W. Chang, *Chem. Mater.* 27 (2015) 6044–6052.
- [14] S.K. Jung, H. Gwon, J. Hong, K.Y. Park, D.H. Seo, H. Kim, J. Hyun, W. Yang, K. Kang, *Adv. Energy Mater.* 4 (2014) 7.
- [15] Y.L. Liang, Y. Yao, *Joule* 2 (2018) 1690–1706.
- [16] F. Zheng, M. Kotobuki, S.F. Song, M.O. Lai, L. Lu, *J. Power Sources* 389 (2018) 198–213.
- [17] L. Fan, S.Y. Wei, S.Y. Li, Q. Li, Y.Y. Lu, *Adv. Energy Mater.* 8 (2018) 31.
- [18] Z.H. Gao, H.B. Sun, L. Fu, F.L. Ye, Y. Zhang, W. Luo, Y.H. Huang, *Adv. Mater.* 30 (2018) 27.
- [19] X.L. Cheng, J. Pan, Y. Zhao, M. Liao, H.S. Peng, *Adv. Energy Mater.* 8 (2018) 16.
- [20] W.Q. Zhang, J.H. Nie, F. Li, Z.L. Wang, C.Q. Sun, *Nano Energy* 45 (2018) 413–419.
- [21] T. Famprikis, P. Canepa, J.A. Dawson, M.S. Islam, C. Masquelier, *Nat. Mater.* (2019) 1–14.
- [22] J. Janek, W.G. Zeier, *Nat. Energy* 1 (2016) 16141.
- [23] L.H. Chen, S. Venkatram, C. Kim, R. Batra, A. Chandrasekaran, R. Ramprasad, *Chem. Mater.* 31 (2019) 4598–4604.
- [24] F.Q. Liu, F.J. Bin, J.X. Xue, L. Wang, Y.J. Yang, H. Huo, J.J. Zhou, L. Li, *ACS Appl. Mater. Interfaces* 12 (2020) 22710–22720.
- [25] S.J. Chen, D.J. Xie, G.Z. Liu, J.P. Mwisizerwa, Q. Zhang, Y.R. Zhao, X.X. Xu, X. Y. Yao, *Energy Storage Mater.* 14 (2018) 58–74.
- [26] P. Hovington, M. Lagace, A. Guerfi, P. Bouchard, A. Manger, C.M. Julien, M. Armand, K. Zaghib, *Nano Lett.* 15 (2015) 2671–2678.
- [27] F. Croce, G.B. Appetecchi, L. Persi, B. Scrosati, *Nature* 394 (1998) 456–458.
- [28] N. Kamaya, K. Homma, Y. Yamakawa, M. Hirayama, R. Kanno, M. Yonemura, T. Kamiyama, Y. Kato, S. Hama, K. Kawamoto, A. Mitsui, *Nat. Mater.* 10 (2011) 682–686.
- [29] Z. Stoeva, I. Martin-Litas, E. Staunton, Y.G. Andreev, P.G. Bruce, *J. Am. Chem. Soc.* 125 (2003) 4619–4626.
- [30] T.W. Pan, D.M. Smith, H. Qi, S.J. Wang, C.Y. Li, *Adv. Mater.* 27 (2015) 5995–6001.
- [31] C.F. Yuan, J. Li, P.F. Han, Y.Q. Lai, Z.A. Zhang, J. Liu, *J. Power Sources* 240 (2013) 653–658.
- [32] K. Hatzell, *Joule* 4 (2020) 719–721.
- [33] C. Monroe, J. Newman, *J. Electrochem. Soc.* 150 (2003) A1377–A1384.
- [34] C. Monroe, J. Newman, *J. Electrochem. Soc.* 151 (2004) A880–A886.
- [35] C. Monroe, J. Newman, *J. Electrochem. Soc.* 152 (2005) A396–A404.
- [36] G.M. Stone, S.A. Mullin, A.A. Teran, D.T. Hallinan, A.M. Minor, A. Hexemer, N. P. Balsara, *J. Electrochem. Soc.* 159 (2012) A222–A227.
- [37] J.F. Wu, E.Y. Chen, Y. Yu, L. Liu, Y. Wu, W.K. Pang, V.K. Peterson, X. Guo, *ACS Appl. Mater. Interfaces* 9 (2017) 1542–1552.
- [38] E. Rangasamy, J. Wolfenstine, J. Sakamoto, *Solid State Ion.* 206 (2012) 28–32.
- [39] F.P. McGrogan, T. Swamy, S.R. Bishop, E. Eggleton, L. Porz, X.W. Chen, Y. M. Chiang, K.J. Van Vliet, *Adv. Energy Mater.* 7 (2017) 5.
- [40] T. Swamy, R. Park, B.W. Sheldon, D. Rettenwander, L. Porz, S. Berendts, R. Uecker, W.C. Carter, Y.M. Chiang, *J. Electrochem. Soc.* 165 (2018) A3648–A3655.
- [41] L. Porz, T. Swamy, B.W. Sheldon, D. Rettenwander, T. Fromling, H.L. Thaman, S. Berendts, R. Uecker, W.C. Carter, Y.M. Chiang, *Adv. Energy Mater.* 7 (2017) 12.
- [42] Q. Zhang, D.X. Cao, Y. Ma, A. Natan, P. Aurora, H.L. Zhu, *Adv. Mater.* 31 (2019).
- [43] P.J. Lian, B.S. Zhao, L.Q. Zhang, N. Xu, M.T. Wu, X.P. Gao, *J. Mater. Chem. A* 7 (2019) 20540–20557.
- [44] H. Lee, P. Oh, J. Kim, H. Cha, S. Chae, S. Lee, J. Cho, *Adv. Mater.* 31 (2019) 26.
- [45] Y. Kato, S. Hori, T. Saito, K. Suzuki, M. Hirayama, A. Mitsui, M. Yonemura, H. Iba, R. Kanno, *Nat. Energy* 1 (2016) 7.
- [46] J. Lau, R.H. DeBlock, D.M. Butts, D.S. Ashby, C.S. Choi, B.S. Dunn, *Adv. Energy Mater.* 8 (2018) 24.
- [47] J. Lee, K. Lee, T. Lee, H. Kim, K. Kim, W. Cho, A. Coskun, K. Char, J.W. Choi, *Adv. Mater.* 32 (2020) 9.
- [48] Z.X. Zhang, L. Zhang, X.L. Yan, H.Q. Wang, Y.Y. Liu, C. Yu, X.T. Cao, L. van Eijck, B. Wen, *J. Power Sources* 410 (2019) 162–170.
- [49] T. Chen, L. Zhang, Z.X. Zhang, P. Li, H.Q. Wang, C. Yu, X.L. Yan, L.M. Wang, B. Xu, *ACS Appl. Mater. Interfaces* 11 (2019) 40808–40816.
- [50] S. Yubuchi, M. Uematsu, C. Hotehama, A. Sakuda, A. Hayashi, M. Tatsumisago, *J. Mater. Chem. A* 7 (2019) 558–566.
- [51] J. Auvergnot, A. Cassel, J.B. Ledeuil, V. Viallet, V. Seznec, R. Dedryvere, *Chem. Mater.* 29 (2017) 3883–3890.
- [52] A. Banerjee, H.M. Tang, X.F. Wang, J.H. Cheng, H. Nguyen, M.H. Zhang, D.H. S. Tang, T.A. Wynn, E.A. Wu, J.M. Doux, T.P. Wu, L. Ma, G.E. Sterbinsky, M. S. D'Souza, S.P. Ong, Y.S. Meng, *ACS Appl. Mater. Interfaces* 11 (2019) 43138–43145.
- [53] D.X. Cao, Y.B. Zhang, A.M. Nolan, X. Sun, C. Liu, J.Z. Sheng, Y.F. Mo, Y. Wang, H. L. Zhu, *Nano Lett.* 20 (2020) 1483–1490.
- [54] J. Park, K.T. Kim, D.Y. Oh, D. Jin, D. Kim, Y.S. Jung, Y.M. Lee, *Adv. Energy Mater.* 10 (2020) 10.
- [55] J.M. Doux, Y.Y.C. Yang, D.H.S. Tan, H. Nguyen, E.A. Wu, X.F. Wang, A. Banerjee, Y.S. Meng, *J. Mater. Chem. A* 8 (2020) 5049–5055.
- [56] J. Zhang, H.Y. Zhong, C. Zheng, Y. Xia, C. Liang, H. Huang, Y.P. Gan, X.Y. Tao, W. K. Zhang, *J. Power Sources* 391 (2018) 73–79.
- [57] J. Zhang, L.J. Li, C. Zheng, Y. Xia, Y.P. Gan, H. Huang, C. Liang, X.P. He, X.Y. Tao, W.K. Zhang, *ACS Appl. Mater. Interfaces* 12 (2020) 41538–41545.
- [58] F. Walther, S. Randau, Y. Schneider, J. Sann, M. Rohnke, F.H. Richter, W.G. Zeier, *J. Janek, Chem. Mater.* 32 (2020) 6123–6136.
- [59] H. Nakamura, T. Kawaguchi, T. Masuyama, A. Sakuda, T. Saito, K. Kuratani, S. Ohsaki, S. Watano, *J. Power Sources* 448 (2020) 10.
- [60] R. Koerver, F. Walther, I. Aygün, J. Sann, C. Dietrich, W.G. Zeier, J. Janek, *J. Mater. Chem. A* 5 (2017) 22750–22760.
- [61] M. Yamamoto, Y. Terauchi, A. Sakuda, A. Kato, M. Takahashi, *J. Power Sources* 473 (2020) 10.
- [62] M. Otoyama, A. Sakuda, M. Tatsumisago, A. Hayashi, *ACS Appl. Mater. Interfaces* 12 (2020) 29228–29234.
- [63] S.J. Choi, S.H. Choi, A.D. Bui, Y.J. Lee, S.M. Lee, H.C. Shin, Y.C. Ha, *ACS Appl. Mater. Interfaces* 10 (2018) 31404–31412.
- [64] D.Y. Oh, D.H. Kim, S.H. Jung, J.G. Han, N.S. Choi, Y.S. Jung, *J. Mater. Chem. A* 5 (2017) 20771–20779.
- [65] H.W. Kwak, Y.J. Park, *Sci. Rep.* 9 (2019) 9.
- [66] X. Li, W. Peng, R. Tian, D. Song, Z. Wang, H. Zhang, L. Zhu, L. Zhang, *Electrochim. Acta* 363 (2020), 137185.
- [67] X.L. Li, H.L. Guan, Z.J. Ma, M. Liang, D.W. Song, H.Z. Zhang, X.X. Shi, C.L. Li, L. F. Jiao, L.Q. Zhang, *J. Energy Chem.* 48 (2020) 195–202.
- [68] X.L. Li, Q.F. Sun, Z.Y. Wang, D.W. Song, H.Z. Zhang, X.X. Shi, C.L. Li, L.Q. Zhang, L.Y. Zhu, *J. Power Sources* 456 (2020) 10.

- [69] G. Peng, X.Y. Yao, H.L. Wan, B.X. Huang, J.Y. Yin, F. Ding, X.X. Xu, *J. Power Sources* 307 (2016) 724–730.
- [70] H. Zhang, X.H. Li, S.M. Hao, X. Zhang, J.P. Lin, *Electrochim. Acta* 325 (2019) 10.
- [71] B.D. McCloskey, *J. Phys. Chem. Lett.* 6 (2015) 4581–4588.
- [72] J. Betz, G. Bieker, P. Meister, T. Placke, M. Winter, R. Schmich, *Adv. Energy Mater.* 9 (2019) 18.
- [73] A. Mukhopadhyay, B.W. Sheldon, *Prog. Mater. Sci.* 63 (2014) 58–116.
- [74] J. Cannarella, C.B. Arnold, *J. Power Sources* 269 (2014) 7–14.
- [75] R. Koerver, W.B. Zhang, L. de Biasi, S. Schweidler, A.O. Kondrakov, S. Kolling, T. Brezesinski, P. Hartmann, W.G. Zeier, J. Janek, *Energy Environ. Sci.* 11 (2018) 2142–2158.
- [76] C.D. Fincher, D. Ojeda, Y.W. Zhang, G.M. Pharr, M. Pharr, *Acta Mater.* 186 (2020) 215–222.
- [77] A. Masias, N. Felten, R. Garcia-Mendez, J. Wolfenstine, J. Sakamoto, *J. Mater. Sci.* 54 (2019) 2585–2600.
- [78] Y.K. Wang, Y.T. Cheng, *Scr. Mater.* 130 (2017) 191–195.
- [79] C. Xu, Z. Ahmad, A. Aryanfar, V. Viswanathan, J.R. Greer, *Proc. Natl. Acad. Sci. U. S. A.* 114 (2017) 57–61.
- [80] S. Narayan, L. Anand, *Extrem. Mech. Lett.* 24 (2018) 21–29.
- [81] Y.T. Cheng, C.M. Cheng, *Mater. Sci. Eng. R.-Rep.* 44 (2004) 91–149.
- [82] L. Greve, C. Fehrenbach, *J. Power Sources* 214 (2012) 377–385.
- [83] E.G. Herbert, S.A. Hackney, N.J. Dudney, P.S. Phani, *J. Mater. Res.* 33 (2018) 1335–1346.
- [84] E.G. Herbert, S.A. Hackney, V. Thole, N.J. Dudney, P.S. Phani, *J. Mater. Res.* 33 (2018) 1361–1368.
- [85] E.G. Herbert, S.A. Hackney, V. Thole, N.J. Dudney, P.S. Phani, *J. Mater. Res.* 33 (2018) 1347–1360.
- [86] R.W. Chang, F.P. McCloskey, *J. Electron. Mater.* 38 (2009) 1855–1859.
- [87] F.J. Wang, X. Ma, Y.Y. Qian, *J. Mater. Sci.* 40 (2005) 1923–1928.
- [88] P. Barai, K. Higa, A.T. Ngo, L.A. Curtiss, V. Srinivasan, *J. Electrochem. Soc.* 166 (2019) A1752–A1762.
- [89] X. Zhang, Q.J. Wang, K.L. Harrison, S.A. Roberts, S.J.J.C.R.P.S. Harris, *Cell. Rep. Phys. Sci.* 1 (2020), 100012.
- [90] H.K. Tian, Y. Qi, *J. Electrochem. Soc.* 164 (2017) E3512–E3521.
- [91] B.N.J. Persson, *Surf. Sci. Rep.* 61 (2006) 201–227.
- [92] P. Barai, K. Higa, V. Srinivasan, *J. Electrochem. Soc.* 164 (2017) A180–A189.
- [93] P. Barai, K. Higa, V. Srinivasan, *J. Electrochem. Soc.* 165 (2018) A2654–A2666.
- [94] K.J. Harry, K. Higa, V. Srinivasan, N.P. Balsara, *J. Electrochem. Soc.* 163 (2016) A2216–A2224.
- [95] J. Zheng, M.S. Kim, Z. Tu, S. Choudhury, T. Tang, L.A. Archer, *Chem. Soc. Rev.* 49 (2020) 2701–2750.
- [96] W.S. LePage, Y.X. Chen, E. Kazyak, K.H. Chen, A.J. Sanchez, A. Poli, E.M. Arruda, M.D. Thouless, N.P. Dasgupta, *J. Electrochem. Soc.* 166 (2019) A89–A97.
- [97] A. Schroeder, J. Fleig, D. Gryaznov, J. Maier, W. Sitte, *J. Phys. Chem. B* 110 (2006) 12274–12280.
- [98] C.T. Love, *J. Electrochem. Energy Convers. Storage* 13 (2016) 5.
- [99] M.B. Dixit, W. Zaman, N. Hortance, S. Vujic, B. Harkey, F.Y. Shen, W.Y. Tsai, V. De Andrade, X.C. Chen, N. Balke, K.B. Hatzell, *Joule* 4 (2020) 207–221.
- [100] A.S. Pandian, X.C. Chen, J.H. Chen, B.S. Lokitz, R.E. Ruther, G. Yang, K. Lou, J. Nanda, F.M. Delnick, N.J. Dudney, *J. Power Sources* 390 (2018) 153–164.
- [101] M.B. Dixit, W. Zaman, Y. Bootwala, Y.J. Zheng, M.C. Hatzell, K.B. Hatzell, *ACS Appl. Mater. Interfaces* 11 (2019) 45087–45097.
- [102] W. Zaman, N. Hortance, M.B. Dixit, V. De Andrade, K.B. Hatzell, *J. Mater. Chem. A* 7 (2019) 23914–23921.
- [103] H.K. Tian, B. Xu, Y. Qi, *J. Power Sources* 392 (2018) 79–86.
- [104] Y.J. Liu, C. Li, B.J. Li, H.C. Song, Z. Cheng, M.R. Chen, P. He, H.S. Zhou, *Adv. Energy Mater.* 8 (2018) 7.
- [105] X.G. Hao, Q. Zhao, S.M. Su, S.Q. Zhang, J.B. Ma, L. Shen, Q.P. Yu, L. Zhao, Y. Liu, F.Y. Kang, Y.B. He, *Adv. Energy Mater.* 9 (2019) 8.
- [106] T. Krauskopf, B. Mogwitz, C. Rosenbach, W.C. Zeier, J. Janek, *Adv. Energy Mater.* 9 (2019) 13.
- [107] J. Kasemchainan, S. Zekoll, D.S. Jolly, Z.Y. Ning, G.O. Hartley, J. Marrow, P. G. Bruce, *Nat. Mater.* 18 (2019) 1105–1110.
- [108] M.J. Wang, R. Choudhury, J. Sakamoto, *Joule* 3 (2019) 2165–2178.
- [109] A.L. Santhosha, L. Medenbach, J.R. Buchheim, P. Adelhelm, *Batter. Supercaps* 2 (2019) 524–529.
- [110] K. Kerman, A. Luntz, V. Viswanathan, Y.M. Chiang, Z. Chen, *J. Electrochem. Soc.* 164 (2017) A1731–A1744.
- [111] W.D. Richards, L.J. Miara, Y. Wang, J.C. Kim, G. Ceder, *Chem. Mater.* 28 (2016) 266–273.
- [112] E.J. Cheng, A. Sharafi, J. Sakamoto, *Electrochim. Acta* 223 (2017) 85–91.
- [113] N.J.J. de Klerk, T. Roslon, M. Wagemaker, *Chem. Mater.* 28 (2016) 7955–7963.
- [114] C. Dietrich, D.A. Weber, S.J. Sedlmaier, S. Indris, S.P. Culver, D. Walter, J. Janek, W.G. Zeier, *J. Mater. Chem. A* 5 (2017) 18111–18119.
- [115] Y.Y. Ren, Y. Shen, Y.H. Lin, C.W. Nan, *Electrochem. Commun.* 57 (2015) 27–30.
- [116] S. Wenzel, T. Leichtweiss, D. Krüger, J. Sann, J. Janek, *Solid State Ion.* 278 (2015) 98–105.
- [117] S. Wenzel, S. Randau, T. Leichtweiss, D.A. Weber, J. Sann, W.G. Zeier, J. Janek, *Chem. Mater.* 28 (2016) 2400–2407.
- [118] L. Xu, S. Tang, Y. Cheng, K.Y. Wang, J.Y. Liang, C. Liu, Y.C. Cao, F. Wei, L.Q. Mai, *Joule* 2 (2018) 1991–2015.
- [119] Y.H. Xiao, Y. Wang, S.H. Bo, J.C. Kim, L.J. Miara, G. Ceder, *Nat. Rev. Mater.* 5 (2020) 105–126.
- [120] L.Z. Sang, R.T. Haasch, A.A. Gewirth, R.G. Nuzzo, *Chem. Mater.* 29 (2017) 3029–3037.
- [121] C. Yu, S. Ganapathy, E.R.H. Van Eck, H. Wang, S. Basak, Z.L. Li, M. Wagemaker, *Nat. Commun.* 8 (2017) 9.
- [122] P. Hartmann, T. Leichtweiss, M.R. Busche, M. Schneider, M. Reich, J. Sann, P. Adelhelm, J. Janek, *J. Phys. Chem. C* 117 (2013) 21064–21074.
- [123] N. Imanishi, S. Hasegawa, T. Zhang, A. Hirano, Y. Takeda, O. Yamamoto, *J. Power Sources* 185 (2008) 1392–1397.
- [124] S.J. Visco, V.Y. Nimon, A. Petrov, K. Pridatko, N. Goncharenko, E. Nimon, L. Jonghe, Y.M. Volkovich, D.A. Bograchev, *J. Solid State Electrochem* 18 (2014) 1443–1456.
- [125] C. Ma, Y.Q. Cheng, K.B. Yin, J. Luo, A. Sharafi, J. Sakamoto, J.C. Li, K.L. More, N. J. Dudney, M.F. Chi, *Nano Lett.* 16 (2016) 7030–7036.
- [126] N.D. Lepley, N.A.W. Holzwarth, Y.J.A. Du, *Phys. Rev. B* 88 (2013).
- [127] T.K. Schwietert, V.A. Arszewska, C. Wang, C. Yu, M. Wagemaker, *Nat. Mater.* 19 (2020) 1–8.
- [128] T. Cheng, B.V. Merinov, S. Morozov, W.A. Goddard, *ACS Energy Lett.* 2 (2017) 1454–1459.
- [129] S. Wenzel, D.A. Weber, T. Leichtweiss, M.R. Busche, J. Sann, J. Janek, *Solid State Ion.* 286 (2016) 24–33.
- [130] R. Garcia-Mendez, F. Mizuno, R.G. Zhang, T.S. Arthur, J. Sakamoto, *Electrochim. Acta* 237 (2017) 144–151.
- [131] A. Sharafi, H.M. Meyer, J. Nanda, J. Wolfenstine, J. Sakamoto, *J. Power Sources* 302 (2016) 135–139.
- [132] K. Ishiguro, Y. Nakata, M. Matsui, I. Uechi, Y. Takeda, O. Yamamoto, N. Imanishi, *J. Electrochem. Soc.* 160 (2013) A1690–A1693.
- [133] E. Kazyak, R. Garcia-Mendez, W.S. LePage, A. Sharafi, A.L. Davis, A.J. Sanchez, K.-H. Chen, C. Haslam, J. Sakamoto, N.P.J.M. Dasgupta, *Matter* 2 (2020) 1025–1048.
- [134] K.B. Hatzell, *Joule* 4 (2020) 719–721.
- [135] Y. Suzuki, K. Kami, K. Watanabe, A. Watanabe, N. Saito, T. Ohnishi, K. Takada, R. Sudo, N. Imanishi, *Solid State Ion.* 278 (2015) 172–176.
- [136] D. Rettenwander, G. Redhammer, F. Preishuber-Pflugl, L. Cheng, L. Miara, R. Wagner, A. Welzl, E. Suard, M.M. Doeffl, M. Wilkening, J. Fleig, G. Amthauer, *Chem. Mater.* 28 (2016) 2384–2392.
- [137] C.L. Tsai, V. Roddatis, C.V. Chandran, Q.L. Ma, S. Uhlenbruck, M. Bram, P. Heitjans, O. Guillon, *ACS Appl. Mater. Interfaces* 8 (2016) 10617–10626.
- [138] R.D. Schmidt, J. Sakamoto, *J. Power Sources* 324 (2016) 126–133.
- [139] L. Porz, T. Swamy, B.W. Sheldon, D. Rettenwander, T. Fromling, H.L. Thaman, S. Berendts, R. Uecker, W.C. Carter, Y.M. Chiang, *Adv. Energy Mater.* 7 (2017) 12.
- [140] N. Seitzman, H. Guthrey, D.B. Sulas, H.A.S. Platt, M. Al-Jassim, S. Pylypenko, *J. Electrochem. Soc.* 165 (2018) A3732–A3737.
- [141] C.H. Wang, K.R. Adair, J.W. Liang, X.N. Li, Y.P. Sun, X. Li, J.W. Wang, Q. Sun, F. P. Zhao, X.T. Lin, R.Y. Li, H. Huang, L. Zhang, R. Yang, S.G. Lu, X.L. Sun, *Adv. Funct. Mater.* 29 (2019) 8.
- [142] J.W. Liang, X.N. Li, Y. Zhao, L.V. Goncharova, W.H. Li, K.R. Adair, M.N. Banis, Y. F. Hu, T.K. Sham, H. Huang, L. Zhang, S.Q. Zhao, S.G. Lu, R.Y. Li, X.L. Sun, *Adv. Energy Mater.* 9 (2019).
- [143] K. Homma, M. Yonemura, M. Nagao, M. Hirayama, R. Kanno, *J. Phys. Soc. Jpn.* 79 (2010) 4.
- [144] M. Murayama, R. Kanno, Y. Kawamoto, T. Kamiyama, *Solid State Ion.* 154 (2002) 789–794.
- [145] M.A. Kraft, S.P. Culver, M. Calderon, F. Bocher, T. Krauskopf, A. Senyshyn, C. Dietrich, A. Zevalkink, J. Janek, W.G. Zeier, *J. Am. Chem. Soc.* 139 (2017) 10909–10918.
- [146] K.H. Park, Q. Bai, D.H. Kim, D.Y. Oh, Y.Z. Zhu, Y.F. Mo, Y.S. Jung, *Adv. Energy Mater.* 8 (2018) 24.
- [147] R. Kanno, M. Maruyama, *J. Electrochem. Soc.* 148 (2001) A742–A746.
- [148] Z.Q. Liu, Y.F. Tang, Y.M. Wang, F.Q. Huang, *J. Power Sources* 260 (2014) 264–267.
- [149] A. Hayashi, S. Hama, F. Mizuno, K. Tadanaga, T. Minami, M. Tatsumisago, *Solid State Ion.* 175 (2004) 683–686.
- [150] B.R. Shin, Y.J. Nam, D.Y. Oh, D.H. Kim, J.W. Kim, Y.S. Jung, *Electrochim. Acta* 146 (2014) 395–402.
- [151] Y.Z. Zhu, X.F. He, Y.F. Mo, *ACS Appl. Mater. Interfaces* 7 (2015) 23685–23693.
- [152] F.D. Han, Y.Z. Zhu, X.F. He, Y.F. Mo, C.S. Wang, *Adv. Energy Mater.* 6 (2016) 9.
- [153] H. Yamane, M. Shibata, Y. Shimane, T. Junke, Y. Seino, S. Adams, K. Minami, A. Hayashi, M. Tatsumisago, *Solid State Ion.* 178 (2007) 1163–1167.
- [154] B.X. Huang, X.Y. Yao, Z. Huang, Y.B. Guan, Y. Jin, X.X. Xu, *J. Power Sources* 284 (2015) 206–211.
- [155] K. Minami, A. Hayashi, M. Tatsumisago, *J. Non-Cryst. Solids* 356 (2010) 2666–2669.
- [156] C. Yu, L. van Eijck, S. Ganapathy, M. Wagemaker, *Electrochim. Acta* 215 (2016) 93–99.
- [157] S. Yubuchi, S. Teragawa, K. Aso, K. Tadanaga, A. Hayashi, M. Tatsumisago, *J. Power Sources* 293 (2015) 941–945.
- [158] E. Rangasamy, Z.C. Liu, M. Gobet, K. Pilar, G. Sahu, W. Zhou, H. Wu, S. Greenbaum, C.D. Liang, *J. Am. Chem. Soc.* 137 (2015) 1384–1387.
- [159] P.F. Zhou, J.B. Wang, F.Y. Cheng, F.J. Li, J. Chen, *Chem. Commun.* 52 (2016) 6091–6094.
- [160] Z.Y. Zhu, I.H. Chu, S.P. Ong, *Chem. Mater.* 29 (2017) 2474–2484.
- [161] F. Wu, W. Fitzhugh, L.H. Ye, J.X. Ning, X. Li, *Nat. Commun.* 9 (2018) 11.
- [162] H. Muramatsu, A. Hayashi, T. Ohtomo, S. Hama, M. Tatsumisago, *Solid State Ion.* 182 (2011) 116–119.
- [163] T. Hakari, M. Nagao, A. Hayashi, M. Tatsumisago, *J. Power Sources* 293 (20) (2015) 721–725.
- [164] G. Sahu, Z. Lin, J.C. Li, Z.C. Liu, N. Dudney, C.D. Liang, *Energy Environ. Sci.* 7 (2014) 1053–1058.

- [165] X. Meng, J. Mater. Chem. A 5 (2017) 18326–18378.
- [166] X.B. Meng, Energy Storage Mater. 30 (2020) 296–328.
- [167] G. Buccì, T. Swamy, Y.M. Chiang, W.C. Carter, J. Mater. Chem. A 5 (2017) 19422–19430.
- [168] L. Porz, T. Swamy, B.W. Sheldon, D. Rettenwander, T. Froemling, H.L. Thaman, S. Berendts, R. Uecker, W.C. Carter, Adv. Energy Mater. 7 (2017) 1701003.
- [169] F. Aguesse, W. Manalastas, L. Buannic, J.M.L. del Amo, G. Singh, A. Llodes, J. Kilner, ACS Appl. Mater. Interfaces 9 (2017) 3808–3816.
- [170] J.P. Yue, Y.G. Guo, Nat. Energy 4 (2019) 174–175.
- [171] F.D. Han, A.S. Westover, J. Yue, X.L. Fan, F. Wang, M.F. Chi, D.N. Leonard, N. Dudney, H. Wang, C.S. Wang, Nat. Energy 4 (2019) 187–196.
- [172] J.M. Doux, H. Nguyen, D.H.S. Tan, A. Banerjee, X.F. Wang, E.A. Wu, C. Jo, H. D. Yang, Y.S. Meng, Adv. Energy Mater. 10 (2020) 6.
- [173] Z. Deng, Z.B. Wang, L.H. Chu, J. Luo, S.P. Ong, J. Electrochem. Soc. 163 (2016) A67–A74.
- [174] Z.Q. Wang, M.S. Wu, G. Liu, X.L. Lei, B. Xu, C.Y. Ouyang, Int. J. Electrochem. Sci. 9 (2014) 562–568.
- [175] W.B. Zhang, D. Schroder, T. Arlt, I. Manke, R. Koerver, R. Pinedo, D.A. Weber, J. Sann, W.G. Zeier, J. Janek, J. Mater. Chem. A 5 (2017) 9929–9936.
- [176] Q. Lemarie, E. Maire, H. Idriissi, P.X. Thivel, F. Alloin, L. Roue, ACS Appl. Energy Mater. 3 (2020) 2422–2431.
- [177] R. Koerver, W. Zhang, L. de Biasi, S. Schweidler, A.O. Kondrakov, S. Kolling, T. Brezesinski, P. Hartmann, W.G. Zeier, J. Janek, Energy Environ. Sci. 11 (2018) 2142–2158.
- [178] W.B. Zhang, D.A. Weber, H. Weigand, T. Arlt, I. Manke, D. Schroder, R. Koerver, T. Leichtweiss, P. Hartmann, W.G. Zeier, J. Janek, ACS Appl. Mater. Interfaces 9 (2017) 17835–17845.
- [179] R. Koerver, I. Aytun, T. Leichtweiss, C. Dietrich, W.B. Zhang, J.O. Binder, P. Hartmann, W.G. Zeier, J. Janek, Chem. Mater. 29 (2017) 5574–5582.
- [180] W.B. Zhang, F.H. Richter, S.P. Culver, T. Leichtweiss, J.G. Lozano, C. Dietrich, P. G. Bruce, W.G. Zeier, J. Janek, ACS Appl. Mater. Interfaces 10 (2018) 22226–22236.
- [181] K. Ishidzu, Y. Oka, T. Nakamura, Solid State Ion. 288 (2016) 176–179.
- [182] A.O. Kondrakov, A. Schmidt, J. Xu, H. Geßwein, R. Mönig, P. Hartmann, H. Sommer, T. Brezesinski, J. Janek, J. Phys. Chem. C 121 (2017) 3286–3294.
- [183] S. Schweidler, L. de Biasi, A. Schiele, P. Hartmann, T. Brezesinski, J. Janek, J. Phys. Chem. C 122 (2018) 8829–8835.
- [184] L. de Biasi, A.O. Kondrakov, H. Geßwein, T. Brezesinski, P. Hartmann, J. Janek, J. Phys. Chem. C 121 (2017) 26163–26171.
- [185] D. Sauersteig, S. Ivanov, H. Reinshagen, A. Bund, J. Power Sources 342 (2017) 939–946.
- [186] B. Rieger, S.V. Erhard, K. Rumpf, A. Jossen, J. Electrochem. Soc. 163 (2016) A1566–A1575.
- [187] D.P. Wilkinson, D. Wainwright, J. Electrochem. Soc. 355 (1993) 193–203.
- [188] F. Strauss, T. Bartsch, L. de Biasi, A.Y. Kim, J. Janek, P. Hartmann, T. Brezesinski, ACS Energy Lett. 3 (2018) 992–996.
- [189] J. Wang, Q.-A. Huang, H. Yu, J. Phys. D: Appl. Phys. 41 (2008), 165406.
- [190] N.C. Rosero-Navarro, T. Kinoshita, A. Miura, M. Higuchi, K. Tadanaga, Ionics 23 (2017) 1619–1624.
- [191] A. Sakuda, A. Hayashi, M. Tatsumisago, Chem. Mater. 22 (2010) 949–956.
- [192] F. Walther, R. Koerver, T. Fuchs, S. Ohno, J. Sann, M. Rohnke, W.G. Zeier, J. Janek, Chem. Mater. 31 (2019) 3745–3755.
- [193] W. Zhang, F.H. Richter, S.P. Culver, T. Leichtweiss, J.G. Lozano, C. Dietrich, P. G. Bruce, W.G. Zeier, J. Janek, ACS Appl. Mater. Interfaces 10 (2018) 22226–22236.
- [194] Z.-J. Zhang, S.-L. Chou, Q.-F. Gu, H.-K. Liu, H.-J. Li, K. Ozawa, J.-Z. Wang, ACS Appl. Mater. Interfaces 6 (2014) 22155–22165.
- [195] K. Takada, T. Inada, A. Kajiyama, H. Sasaki, S. Kondo, M. Watanabe, M. Murayama, R. Kanno, Solid State Ion. 158 (2003) 269–274.
- [196] N. Ohta, K. Takada, I. Sakaguchi, L. Zhang, R. Ma, K. Fukuda, M. Osada, T. Sasaki, Electrochem. Commun. 9 (2007) 1486–1490.
- [197] Y. Seino, K. Takada, B.-C. Kim, L. Zhang, N. Ohta, H. Wada, M. Osada, T. Sasaki, Solid State Ion. 176 (2005) 2389–2393.
- [198] R. Franke, T. Chassé, P. Streubel, A. Meisel, JESRA 56 (1991) 381–388.
- [199] J. Zhang, C. Zheng, L.J. Li, Y. Xia, H. Huang, Y.P. Gan, C. Liang, X.P. He, X.Y. Tao, W.K. Zhang, Adv. Energy Mater. 10 (2020) 12.
- [200] D. Goonetilleke, N. Sharma, W.K. Pang, V.K. Peterson, R. Petibon, J. Li, J.R. Dahn, Chem. Mater. 31 (2019) 376–386.
- [201] H.Y. Li, J. Li, N. Zaker, N. Zhang, G.A. Botton, J.R. Dahn, J. Electrochem. Soc. 166 (2019) A1956–A1963.
- [202] J. Li, H.Y. Li, W. Stone, R. Weber, S. Hy, J.R. Dahn, J. Electrochem. Soc. 164 (2017) A3529–A3537.
- [203] G.N. Qian, Y.T. Zhang, L.S. Li, R.X. Zhang, J.M. Xu, Z.J. Cheng, S.J. Xie, H. Wang, Q.L. Rao, Y.S. He, Y.B. Shen, L.W. Chen, M. Tang, Z.F. Ma, Energy Storage Mater. 27 (2020) 140–149.
- [204] S. Wolff-Goodrich, F. Lin, I.M. Markus, D. Nordlund, H.L. Xin, M. Asta, M. M. Doeff, Phys. Chem. Chem. Phys. 17 (2015) 21778–21781.
- [205] D.C. Li, C.Q. Yuan, J.Q. Dong, Z.H. Peng, Y.H. Zhou, J. Solid State Electrochem 12 (2008) 323–327.
- [206] J.W. Fergus, J. Power Sources 195 (2010) 939–954.
- [207] T. Shi, Q.S. Tu, Y.S. Tian, Y.H. Xiao, L.J. Miara, O. Kononova, G. Ceder, Adv. Energy Mater. 10 (2020) 9.
- [208] K.H. Nie, Y.S. Hong, J.L. Qiu, Q.H. Li, X.Q. Yu, H. Li, L.Q. Chen, Front. Chem. 6 (2018) 19.
- [209] S.A. Peryez, M.A. Cambaz, V. Thangadurai, M. Fichtner, ACS Appl. Mater. Interfaces 11 (2019) 22029–22050.
- [210] K. Fu, Y.H. Gong, G.T. Hitz, D.W. McOwen, Y.J. Li, S.M. Xu, Y. Wen, L. Zhang, C. W. Wang, G. Pastel, J.Q. Dai, B.Y. Liu, H. Xie, Y.G. Yao, E.D. Wachsman, L.B. Hu, Energy Environ. Sci. 10 (2017) 1568–1575.
- [211] X.Y. Yao, N. Huang, F.D. Han, Q. Zhang, H.L. Wan, J.P. Mzwirwa, C.S. Wang, X. X. Xu, Adv. Energy Mater. 7 (2017) 9.
- [212] J.N. Reimers, J.R. Dahn, J. Electrochem. Soc. 139 (1992) 2091–2097.
- [213] Q. Yao, S.-L. Shang, Y.-J. Hu, Y. Wang, Y. Wang, Y.-H. Zhu, Z.-K. Liu, Intermetallics 78 (2016) 1–7.
- [214] J. Janek, M. Martin, K.D. Becker, Phys. Chem. Chem. Phys. 11 (2009), 3010–3010.
- [215] C. Liang, R.C. Longo, F. Kong, C. Zhang, Y. Nie, Y. Zheng, J.-S. Kim, S. Jeon, S. Choi, K. Cho, J. Power Sources 340 (2017) 217–228.
- [216] J. Li, R. Shunmugasundaram, R. Doig, J.R. Dahn, Chem. Mater. 28 (2016) 162–171.
- [217] J. Li, R. Petibon, S. Glazier, N. Sharma, W.K. Pang, V.K. Peterson, J.R. Dahn, Electrochim. Acta 180 (2015) 234–240.
- [218] I. Buchberger, S. Seidlmayer, A. Pokharel, M. Piana, J. Hattendorff, P. Kudejova, R. Gilles, H.A. Gasteiger, J. Electrochem. Soc. 162 (2015) A2737–A2746.
- [219] J. Li, L.E. Downie, L. Ma, W. Qiu, J.R. Dahn, J. Electrochem. Soc. 162 (2015) A1401–A1408.
- [220] C. Ghanty, B. Markovsky, E.M. Erickson, M. Talianker, O. Haik, Y. Tal-Yossef, A. Mor, D. Aurbach, J. Lampert, A. Volkov, J.-Y. Shin, A. Garsuch, F.F. Chesneau, C. Erk, ChemElectroChem 2 (2015) 1479–1486.
- [221] T.Y. Liu, Z.J. Du, X.Y. Wu, M.M. Rahman, D. Nordlund, K.J. Zhao, M.D. Schulz, F. Lin, D.L. Wood, I. Belharouak, Chem. Commun. 56 (2020) 6973–6976.
- [222] S. Vadivel, N. Phattharasupakun, J. Wutthiprom, S. Duangdangchote, M. Sawangphruk, ACS Appl. Mater. Interfaces 11 (2019) 30719–30727.
- [223] D.Y. Wan, Z.Y. Fan, Y.X. Dong, E. Baasanjav, H.B. Jun, B. Jin, E.M. Jin, S. M. Jeong, J. Nanomater. 2018 (2018) 9.
- [224] S.H. Jung, U.H. Kim, J.H. Kim, S.G. Jun, C.S. Yoon, Y.S. Jung, Y.K. Sun, Adv. Energy Mater. 10 (2020) 12.
- [225] D.J. Miller, C. Proff, J.G. Wen, D.P. Abraham, J. Bareno, Adv. Energy Mater. 3 (2013) 1098–1103.
- [226] P.F. Yan, J.M. Zheng, M. Gu, J. Xiao, J.G. Zhang, C.M. Wang, Nat. Commun. 8 (2017) 9.
- [227] J.Y. Li, A. Manthiram, Adv. Energy Mater. 9 (2019) 14.
- [228] W.D. Li, H.Y. Asl, Q. Xie, A. Manthiram, J. Am. Chem. Soc. 141 (2019) 5079–5101.
- [229] J.H. Park, J.H. Cho, S.B. Kim, W.S. Kim, S.Y. Lee, S.Y. Lee, J. Mater. Chem. 22 (2012) 12574–12581.
- [230] S. Yoon, K.N. Jung, S.H. Yeon, C.S. Jin, K.H. Shin, J. Electroanal. Chem. 683 (2012) 88–93.
- [231] Q.W. Ran, H.Y. Zhao, Y.Z. Hu, Q.Q. Shen, W. Liu, J.T. Liu, X.H. Shu, M.L. Zhang, S.S. Liu, M. Tan, H. Li, X.Q. Liu, Electrochim. Acta 289 (2018) 82–93.
- [232] X.H. Xiong, D. Ding, Z.X. Wang, B. Huang, H.J. Guo, X.H. Li, J. Solid State Electrochem 18 (2014) 2619–2624.
- [233] B.H. Song, W.D. Li, S.M. Oh, A. Manthiram, ACS Appl. Mater. Interfaces 9 (2017) 9718–9725.
- [234] P.F. Yan, J.M. Zheng, J. Liu, B.Q. Wang, X.P. Cheng, Y.F. Zhang, X.L. Sun, C. M. Wang, J.G. Zhang, Nat. Energy 3 (2018) 600–605.
- [235] X.M. Fan, G.R. Hu, B. Zhang, X. Ou, J.F. Zhang, W.G. Zhao, H.P. Jia, L.F. Zou, P. Li, Y. Yang, Nano Energy 70 (2020) 11.
- [236] X.S. Liu, B.Z. Zheng, J. Zhao, W.M. Zhao, Z.T. Liang, Y. Su, C.P. Xie, K. Zhou, Y. X. Xiang, J.P. Zhu, H.C. Wang, G.M. Zhong, Z.L. Gong, J.Y. Huang, Y. Yang, 202003583, Adv. Energy Mater. (2021) 11.
- [237] R. Cao, J. Qian, J.-G. Zhang, W. Xu (Eds.), Rechargeable Batteries, Springer, 2015, pp. 637–671.
- [238] Y.G. Lee, S. Fujiki, C. Jung, N. Suzuki, N. Yashiro, R. Omoda, D.S. Ko, T. Shiratsuchi, T. Sugimoto, S. Ryu, J.H. Ku, T. Watanabe, Y. Park, Y. Aihara, D. Im, I.T. Han, Nat. Energy 5 (2020) 299–308.
- [239] X. Ji, S.Y. Hou, P.F. Wang, X.Z. He, N. Piao, J. Chen, X.L. Fan, C.S. Wang, Adv. Mater. 32 (2020) 9.
- [240] J. Yang, B.X. Huang, J.Y. Yin, X.Y. Yao, G. Peng, J. Zhou, X.X. Xu, J. Electrochem. Soc. 163 (2016) A1530–A1534.
- [241] X.L. Li, L.B. Jin, D.W. Song, H.Z. Zhang, X.X. Shi, Z.Y. Wang, L.Q. Zhang, L.Y. Zhu, J. Energy Chem. 40 (2020) 39–45.
- [242] B. Emlay, Y.L. Liang, R. Chen, C.S. Wu, M. Pan, Z. Fan, Y. Yao, Mater. Today Phys. 18 (2021), 100397.